Synthetic scientific report

on the implementation of the project PN-II-ID-PCE-2011-3-0224 in the period October 2011 – September 2016

The project PN-II-ID-PCE-2011-3-0224, entitled

Analogies between electron transport in nanostructures and light propagation

is focused on the detailed study of analogies between the transport of charge carriers in nanostructures and the propagation of electromagnetic waves, with the aim of developing analogies that have not been evidenced theoretically and/or experimentally up to now. The studied nanostructures include common semiconductors, in which electrons are described by the Schrödinger equation and graphene, in which electrons satisfy a Dirac-type equation. In the first case, the analogies are justified by the formal similarity between the time-independent Schrödinger equation and the Helmholtz equation, while in the second case the spinorial wavefunction in graphene can be put into correspondence with the polarized states of light, the components of the electromagnetic field, or the light propagation in hexagonal photonic crystals that show no bandgap. The aim is that, by emphasizing the differences and similarities between the propagation of electrons and photons, to contribute to the development of new devices based on the electron-photon analogy, and to understand better the charge transport in disordered nanostructures with an inhomogeneous distribution of scattering centers.

The project started with the study of analogies between ballistic electrons described by either Schrödinger or Dirac equations and light (2011-2012), while the work developed in the period 2012-2013 is dedicated to numerical simulations and experimental investigations of electron transport in disordered nanostructures, with an inhomogeneous distribution of the scattering centers.

Results obtained in the 2011 stage of the project

In 2011 we focused on the effects of light polarization on the analogies ballistic electron-electromagnetic field, corresponding to the activity 1.1 in the project. Ballistic transport takes place in nanostructures with dimensions smaller than the average distance between two successive collisions of an electron with other electrons or with the impurities in the semiconductor.

The polarization of the electromagnetic field influences light propagation through the boundary conditions at the interface between media with different parameters (in particular, refractive indices).

The influence of polarization on the analogies between light and Schrödinger ballistic electrons

Under stationary transport conditions, the wavefunction Ψ of ballistic electrons with effective mass *m* and constant energy *E* in common semiconductors satisfies the time-independent Schrödinger equation

$$-\frac{\hbar^2}{2m}\nabla^2\Psi + (V-E)\Psi = 0 \qquad (1)$$

where *V* is the potential energy. This equation is formally similar with the Helmholtz equation satisfied by monochromatic light beams with frequency ω and wavevector ***k*** in media with constant and isotropic electric permittivity ε and magnetic permeability μ [1]:

$$\nabla^2\boldsymbol{F} + k^2\boldsymbol{F} = 0\,. \qquad (2)$$

In (2), ***F*** stands for any component of the electric ***E*** or magnetic ***H*** fields, and $k = \omega\sqrt{\varepsilon\mu} = |\,\boldsymbol{k}\,|$. The vectors ***E***, ***H*** and ***k*** are orthogonal and form a right-handed system.

Although, as follows from (1) and (2), Ψ is similar to any component of the fields ***E*** and ***H*** if ***k*** is replaced by the electron wavevector $\boldsymbol{\gamma}$, where $|\,\boldsymbol{\gamma}\,| = \gamma = \sqrt{2m(E-V)}/\hbar$, the quantitative analogies between the set of relevant parameters for electrons, *m* and $(E-V)$, and those for light (ω, ε and μ) at propagation through a succession of different regions, as in Fig. 1, depend on the polarization of the electromagnetic field, which

determines the continuity conditions at interface. Besides these conditions we impose the equality of the group velocity, given by $1/\sqrt{\varepsilon\mu}$ for plane electromagnetic waves, and, respectively, $\mathrm{Re}[i\hbar\Psi\cdot\nabla\Psi^*/m]/|\Psi|^2=\hbar\gamma/m$ for electrons.

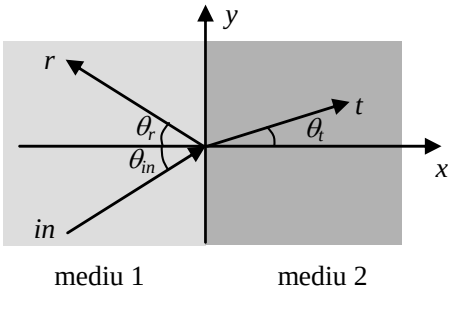

Fig. 1

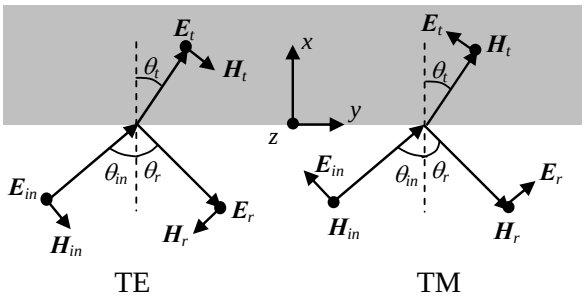

Fig. 2

We consider electromagnetic fields/electron beams propagating in the (*xy*) plane, and label with indices 1 and 2 the respective parameter values in the incidence medium 1 and transmission medium 2. Irrespective of light polarization, the tangential components of $\boldsymbol{k}$ and $\boldsymbol{\gamma}$ are conserves, according to the Snell law, which can be expressed as

$$k_1\sin\theta_{in}=k_1\sin\theta_r=k_2\sin\theta_t\,,\qquad \gamma_1\sin\theta_{in}=\gamma_1\sin\theta_r=\gamma_2\sin\theta_t\,, \tag{3}$$

from which it follows that $\theta_r=\theta_{in}$. In (3) θ_{in}, θ_r and θ_t are the angles of incidence, reflection and transmission of the electromagnetic field/electron beam. Other continuity conditions, dependent on light polarization, require the conservation of the tangential components of $\boldsymbol{E}$ and $\boldsymbol{H}$, whereas for electrons Ψ and $(\nabla\Psi\cdot\hat{\boldsymbol{x}})/m$ must be continuous at the interface, with $\hat{\boldsymbol{x}}$ the versor along the *x* direction.

Until now, a set of analogous parameters for the propagation of electrons and of light were found only when the electromagnetic radiation is polarized TE (transverse electric) or TM (transverse magnetic) [1]. The orientations of the fields $\boldsymbol{E}$ and $\boldsymbol{H}$ for the polarizations TE and TM are illustrated in Fig. 2. In both cases, the electronic wavefunction can be put into correspondence with the vector potential $\boldsymbol{A}$ of the electromagnetic field, which satisfies equation (2) [2] and is related $\boldsymbol{E}$ and $\boldsymbol{H}$ as $\boldsymbol{E}=-i\omega\boldsymbol{A}$ and, respectively, $\boldsymbol{H}=(\nabla\times\boldsymbol{A})/\mu$ if the scalar potential of the electromagnetic radiation vanishes.

In the 2011 stage of the project, we have studied the analogy between the scalar electron wavefunction and the vector potential of a light wave linearly polarized at an angle α with respect to the *z* axis. The case α = 0 corresponds to a TE wave, while $\alpha=\pi/2$ describes a TM wave. In order to obtain a set of analogies for different values of α, we had to find first a new set of analogous parameters for the TE and TM waves, because in [2] the effective mass, electron energy and even the wavefunction were equivalent to parameters with different dimensionalities for the TE and TM cases.

In this respect, we have expressed the incident, reflected and transmitted electron wavefunction components as

$$\Psi_{in}\exp[i\gamma_1(x\cos\theta_{in}+y\sin\theta_{in})],\quad \Psi_r\exp[i\gamma_1(-x\cos\theta_r+y\sin\theta_r)],\quad \Psi_t\exp[i\gamma_2(x\cos\theta_t+y\sin\theta_t)], \tag{4}$$

and analogous for the TE wave:

$$A_{in}\hat{\boldsymbol{z}}\exp[ik_1(x\cos\theta_{in}+y\sin\theta_{in})],\ A_r\hat{\boldsymbol{z}}\exp[ik_1(-x\cos\theta_r+y\sin\theta_r)],\ A_t\hat{\boldsymbol{z}}\exp[ik_2(x\cos\theta_t+y\sin\theta_t)]. \tag{5}$$

From the continuity conditions at *x* = 0 for the electron wavefunction and the tangential components of $\boldsymbol{E}$ and $\boldsymbol{H}$ we obtain

$$\begin{cases}\Psi_{in}+\Psi_r=\Psi_t\\ \dfrac{\gamma_1}{m_1}\cos\theta_{in}(\Psi_{in}-\Psi_r)=\dfrac{\gamma_2}{m_2}\cos\theta_t\Psi_t\end{cases}\qquad\qquad \begin{cases}A_{in}+A_r=A_t\\ \dfrac{k_1}{\mu_1}\cos\theta_{in}(A_{in}-A_r)=\dfrac{k_2}{\mu_2}\cos\theta_tA_t\end{cases} \tag{6}$$

at which we add the similarities between *k* and γ and between the group velocities $1/\sqrt{\varepsilon\mu}$ and $\hbar\gamma/m$. These similarities lead to the set of analogies in Table 1, where the effective mass, electric permittivity and magnetic permeability were written as products: $m = m_0 m_r$, $\varepsilon = \varepsilon_0\varepsilon_r$, $\mu = \mu_0\mu_r$, with m_0 the free electron mass and ε_0 and μ_0 the dielectric constants of the vacuum, the parameters labeled with *r* denoting relative values. The refractive index of the electromagnetic field is defined as $n = \sqrt{\varepsilon_r\mu_r}$.

Table 1. Set of analogous ballistic electron-light parameters for electromagnetic fields with different polarizations

Electronic wavefunction	Electromagnetic field		
	TE	TM	Polarized at an angle α
Ψ	A	$\sqrt{\varepsilon_r/\mu_r}A$	$\sqrt{A_{\parallel}^2 + (\varepsilon_r/\mu_r)A_{\perp}^2}\exp[i\arctan(\sqrt{\varepsilon_r/\mu_r}\tan\alpha)]$
$2(E-V)/\hbar$	ω	ω	ω
$E/(E-V)$	ε_r	μ_r	$\sqrt{\varepsilon_r\mu_r}\sqrt{(\varepsilon_r\cos^2\alpha + \mu_r\sin^2\alpha)/(\mu_r\cos^2\alpha + \varepsilon_r\sin^2\alpha)}$
m_r	μ_r	ε_r	$\sqrt{\varepsilon_r\mu_r}\sqrt{(\mu_r\cos^2\alpha + \varepsilon_r\sin^2\alpha)/(\varepsilon_r\cos^2\alpha + \mu_r\sin^2\alpha)}$
$m_0/2E$	$\varepsilon_0\mu_0$	$\varepsilon_0\mu_0$	$\varepsilon_0\mu_0$

Similarly, for TM polarization, the incident, reflected and transmitted vector potentials are

$$A_{in}(\hat{\boldsymbol{x}}\sin\theta_{in} - \hat{\boldsymbol{y}}\cos\theta_{in})\exp[ik_1(x\cos\theta_{in} + y\sin\theta_{in})], \quad A_r(\hat{\boldsymbol{x}}\sin\theta_r + \hat{\boldsymbol{y}}\cos\theta_r)\exp[ik_1(-x\cos\theta_r + y\sin\theta_r)],$$
$$A_t(\hat{\boldsymbol{x}}\sin\theta_t - \hat{\boldsymbol{y}}\cos\theta_t)\exp[ik_2(x\cos\theta_t + y\sin\theta_t)]. \tag{7}$$

and the continuity conditions at the interface for the tangential components of ***E*** and ***H*** require that

$$\begin{cases} \dfrac{k_1}{\mu_1}(A_{in} + A_r) = \dfrac{k_2}{\mu_2}A_t \\ \cos\theta_{in}(A_{in} - A_r) = \cos\theta_t A_t \end{cases} \tag{8}$$

The new set of analogous parameters for electrons and the electromagnetic field is presented in Table 1. As can be seen, the analogous parameters for the TE and TM cases have now the same dimensionality.

A more complicated situation is encountered for a linearly polarized wave at an angle α with respect to the *z* axis. In this case, if we denote with $A_{\parallel} = A\cos\alpha$ and $A_{\perp} = A\sin\alpha$, the vector potentials of the incident, reflected and transmitted waves can be written as

$$[A_{\parallel,in}\hat{\boldsymbol{z}} + A_{\perp,in}(\hat{\boldsymbol{x}}\sin\theta_{in} - \hat{\boldsymbol{y}}\cos\theta_{in})]\exp[ik_1(x\cos\theta_{in} + y\sin\theta_{in})],$$
$$[A_{\parallel,r}\hat{\boldsymbol{z}} + A_{\perp,r}(\hat{\boldsymbol{x}}\sin\theta_r + \hat{\boldsymbol{y}}\cos\theta_r)]\exp[ik_1(-x\cos\theta_r + y\sin\theta_r)], \tag{9}$$
$$[A_{\parallel,t}\hat{\boldsymbol{z}} + A_{\perp,t}(\hat{\boldsymbol{x}}\sin\theta_t - \hat{\boldsymbol{y}}\cos\theta_t)]\exp[ik_2(x\cos\theta_t + y\sin\theta_t)],$$

and the interface conditions are

$$\begin{cases} (A_{\parallel,in} + A_{\parallel,r})\hat{\boldsymbol{z}} - (A_{\perp,in} - A_{\perp,r})\hat{\boldsymbol{y}}\cos\theta_{in} = A_{\parallel,t}\hat{\boldsymbol{z}} - A_{\perp,t}\hat{\boldsymbol{y}}\cos\theta_t \\ \sqrt{\varepsilon_{r,1}/\mu_{r,1}}[(A_{\perp,in} + A_{\perp,r})\hat{\boldsymbol{z}} + (A_{\parallel,in} - A_{\parallel,r})\hat{\boldsymbol{y}}\cos\theta_{in}] = \sqrt{\varepsilon_{r,2}/\mu_{r,2}}[A_{\perp,t}\hat{\boldsymbol{z}} + A_{\parallel,t}\hat{\boldsymbol{y}}\cos\theta_t] \end{cases} \tag{10}$$

The requirements (6, left) and (10) do not allow the direct finding of a set of analogous parameters because in (10) there are terms that depend on cos(.) and other independent of this function. However, a set of electron-light analogous parameters can be obtained (see Table 1) by adding the two equations in (10) and

comparing the result to the interface conditions for electrons. To emphasize the different character of the terms with the same orientation obtained in this manner, the second equation in (10) was first multiplied by the imaginary number *i*, which allowed the equivalence between the electronic wavefunction and a complex number.

As can be seen from Table 1, from the set of parameters for a linearly polarized light field at angle α one can obtain the corresponding sets for TE and TM polarizations in the appropriate limits. But, unlike for TE and TM cases, this set of parameters cannot be directly used to design optical structures with the same reflection and transmission coefficients, *R* and *T*, as the corresponding nanostructures for electrons because *R* for a linearly polarized field at angle α is given by [3]

$$R = |A_r / A_{in}|^2 = (\cos\alpha)^2 R_{TE} + (\sin\alpha)^2 R_{TM} = (\cos\alpha)^2 |A_{\parallel,r} / A_{\parallel,in}|^2 + (\sin\alpha)^2 |A_{\perp,r} / A_{\perp,in}|^2 \quad (11)$$

i.e. is obtained by treating independently the TE and TM components.

The angle α is, however, a parameter that can be easily tuned experimentally in optical structures to simulate the propagation of ballistic electrons with different energies. For instance, in Fig. 3 we have represented the dependence on energy and incidence angle of the reflection coefficient for an electron beam with $V_1 = 0$, $V_2 = 0.2$ eV, $m_1 = 0.08\, m_0$, and $m_2 = 0.15\, m_0$, while in Fig. 4 we have displayed the dependence of *R* on α and θ_{in} at an interface between two non-magnetic media with $n_1 = 1$, $n_2 = 2.5$. In both cases higher values correspond to darker colours (*R* takes values between 0 and 1).

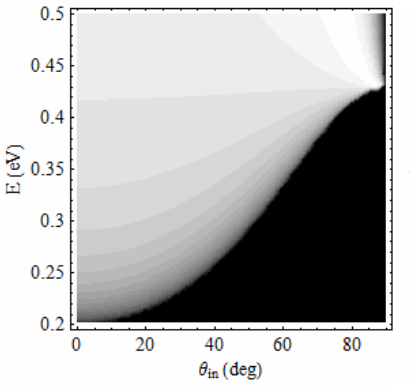

Fig. 3

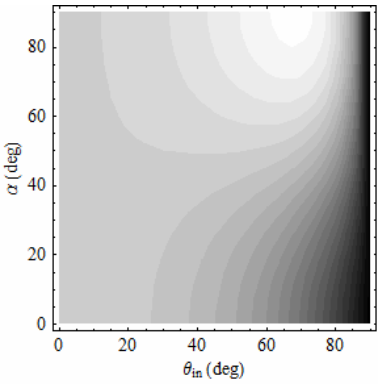

Fig. 4

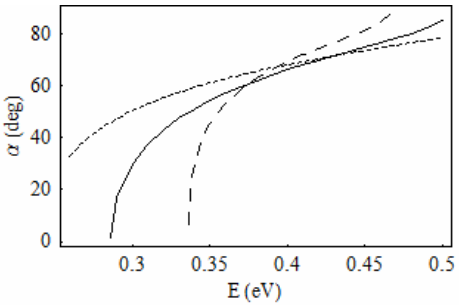

Fig. 5

The same reflection coefficient *R* for the electromagnetic field and electron beam can be obtained by correlating the parameters α and *E*. For example, in Fig. 5 we have represented such a correlation for the case above of electrons/light incident at the angles 40°/50° (solid line), 15°/50° (dotted line) and 60°/77° (dashed line). It should be emphasized that the choice of different incident angles for electrons and light makes it easier to choose optimal parameters for quantum/optical systems with the same *R*.

Influence of polarization on the analogies between electromagnetic field and the spinorial electron wavefunction in graphene

Because of the vanishing effective mass of charge carriers in graphene and of their linear dispersion relation, similar to the case of photons, the analogy between the propagation of charge carriers in graphene and the electromagnetic field seems to be more straightforward. However, up to now no set of analogous graphene/light parameters was found since the charge carriers in graphene have a quantum property with no classical analog: chirality.

Graphene is a bidimensional crystal, assumed to extend in the plane (*xy*), and consisting of a periodic hexagonal arrangement of carbon atoms [4]. The spinorial wavefunction in graphene, with components $\Psi^T = (\psi_1, \psi_2)$ (*T* indicates transposition), satisfies the equation

$$\hbar v_F \begin{pmatrix} 0 & \gamma_x - i\gamma_y \\ \gamma_x + i\gamma_y & 0 \end{pmatrix} \begin{pmatrix} \psi_1 \\ \psi_2 \end{pmatrix} = (E - V) \begin{pmatrix} \psi_1 \\ \psi_2 \end{pmatrix} \quad (12)$$

where $v_F \cong c/300$ is the Fermi velocity and γ_x and γ_y are the components of the charge carrier wavevector $\boldsymbol{\gamma}$ along the directions *x* and *y*, with wavenumber $\gamma = |\boldsymbol{\gamma}|$. The dispersion relation obtained from (12) is linear: $E = V \pm \hbar v_F |\boldsymbol{\gamma}|$, the positive and negative signs corresponding to electron and hole states, respectively.

The reflection coefficient at an interface between two regions with different potential energies is found by expressing the wavefunction in each region as a superposition of forward- and backward-propagating components:

$$\begin{pmatrix} \psi_1 \\ \psi_2 \end{pmatrix} = \exp(i\gamma y \sin\theta) \begin{pmatrix} A\exp(i\gamma x\cos\theta) + B\exp(-i\gamma x\cos\theta) \\ s[A\exp(i\gamma x\cos\theta + i\theta) - B\exp(-i\gamma x\cos\theta - i\theta)] \end{pmatrix} \tag{13}$$

and imposing the boundary condition that Ψ is constant at the interface. In (13), $s = \mathrm{sgn}(E - V)$. The Snell law becomes

$$(E - V_1)\sin\theta_1 = (E - V_2)\sin\theta_2 \tag{14}$$

and the reflection coefficient can be written as

$$R = \left| \frac{s_1 \exp(i\theta_1) - s_2 \exp(i\theta_2)}{s_1 \exp(-i\theta_1) + s_2 \exp(i\theta_2)} \right|^2 \tag{15}$$

The spinoriala wavefunction in graphene has been put into correspondence with the polarized states of light [5], or with a TE electromagnetic field [6], but no similar graphene/light boundary conditions/set of analogous parameters was identified. The analogy graphene/polarized light at angle α was studied for the first time in the 2011 stage of this project.

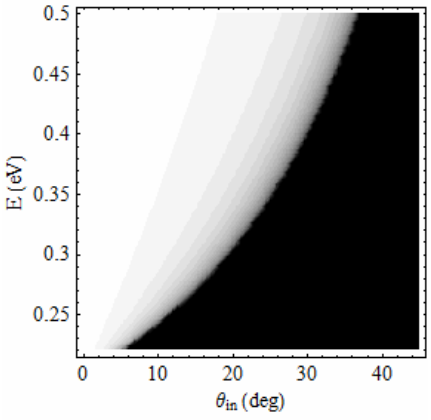

Fig. 6

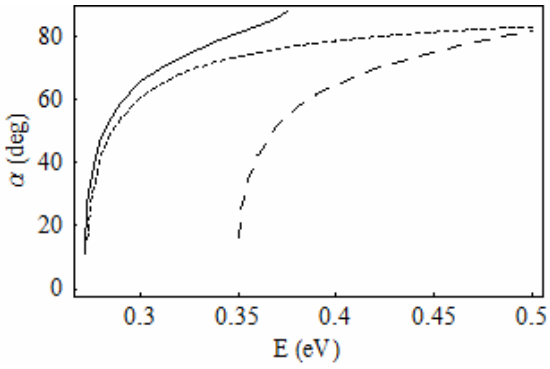

Fig. 7

In a similar manner to the case of Schrödinger electrons, a correlation between *E* and α can be found also in this case. In Fig. 6 we have presented the dependence on the incidence angle and energy of the reflection coefficient of electrons in graphene for V_1 =0, V_2 = 0.2 eV, and in Fig. 7 we have illustrated the correlation between *E* and α to obtain the same *R* as in the optical case, with the same parameters as above, in Fig. 4. The solid, dotted and dashed lines correspond to electrons/light incident at angles 15°/75°, 15°/70° and 25°/75°, respectively. As can be seen from Fig. 7, the same *R* as for electrons can be obtained in the optical case in a wider or narrower range of *E* for different incidence angles for the electromagnetic field. The energy range *E* is chosen such that the charge carriers in graphene are electrons; a similar treatment holds for holes, which transport electric charge for *E* < 0. Moreover, Fig. 7 shows that the quantitative electron/light analogy on a wide energy range cannot always exist for a single incident angle. For instance, to obtain the *R* range for electrons with energies between 0.2 eV and 0.5 eV, the optical analog needs to be illuminated at two incidence angles, in each case the polarization being tuned such that the range of the reflection coefficient is the same as for electrons (see, for example, the solid line, for which no solution for α exist for energies *E* higher than 0.36 eV).

Although in the simulations above, irrespective of the equation satisfied by electrons (Schrödinger or Dirac), only one interface between media with different characteristics was considered, the results can be generalized for a succession of regions with different widths if, besides the equality condition for the reflection coefficient at each interface, the phase matching requirement:

$$k \cos\theta_{opt} L_{opt} = \gamma \cos\theta_{el} L_{el} \qquad (16)$$

is also imposed, where the indices *opt* and *el* refer to the optical and electronic case, respectively, and L_{opt}, L_{el} are the widths of the regions traversed by optical and electron beams.

Unlike the set of analogous electron/light parameters used up to now, which required the variation of light frequency or refractive indices to obtain the same *R* as for electrons propagating through a succession of regions with different parameters, the identification of light polarization as an easily controllable parameter in experiments offer the possibility to design simpler optical structures with the same reflection and transmission characteristics as the corresponding ballistic nanostructures.

The results obtained in the 2011 stage of the project were published in an ISI journal (publication [P1]).

Results obtained in the 2012 stage of the project

In the 2012 stage we have studied the analogies related to the activities 1.2 (Analogies between optics and the propagation of electrons in anisotropic media/type II heterostructures), 1.3 (Analogies between light propagation in metamaterials and nanostructures), and 1.4 (Analogies between spin/applied magnetic field in nanostructures and polarized states of light) of the project. In addition, we have developed algorithms for simulating inhomogeneous and disordered nanostructures.

Analogies between electromagnetic field and ballistic Schrödinger electrons in anisotropic media/type II heterostructures, metamaterials or in the presence of spin effects

Regarding activity 1.2, based on the analogy with amphoteric light refraction [7], we have demonstrated that at the interface between an isotropic medium, denoted by 1, and an anisotropic one, denoted by 2 (see Fig. 8) the current density of electrons, ***j***, is refracted at an angle ϕ_2, which is different from the refraction angle θ_2 of the wavevector ***k***, these angles being identical in the isotropic medium 1: $\phi_1 = \theta_1$. In particular, at the interface between the isotropic crystal Bi_2Se_3 and the anisotropic crystal Bi_2Te_3, when the ellipsoid of the effective mass is oblique with respect to the interface, the signs of the angles ϕ_2 and θ_2 can differ for a wide range of incidence angles (see Fig. 9), the transmission coefficient of electrons having significant values in the whole range, as can be seen from Fig. 10.

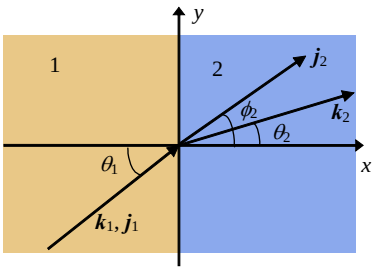

Fig. 8

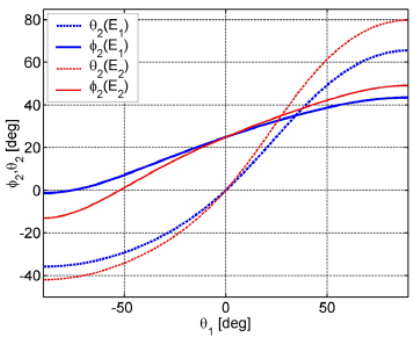

Fig. 9

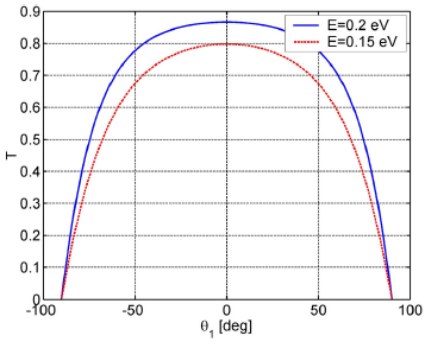

Fig. 10

As an application, we have shown that a point-like electron source, with an angular divergence of 60° can be collimated after refraction at the interface Bi_2Se_3/Bi_2Te_3 situated at *x* = 4 nm in Fig. 11, its divergence $\Delta\phi_2 = \phi_2(30°) - \phi_2(-30°)$ being smaller than the initial value. In addition, the electron beam propagates now at an angle $\phi_{st} = [\phi_2(30°) + \phi_2(-30°)]/2$. The electron trajectories are represented with red lines in Fig. 11, the blue lines indicating the virtual electron source, and the dependences on the electron energy of the angles $\Delta\phi_2$ and ϕ_{st} are illustrated in Fig. 12. Figure 13 represents the probability of finding an electron

that passes through the interface situated at x = 4 nm, the oscillations in the left part of the figure indicating the interference between the incident and reflected wavefunctions.

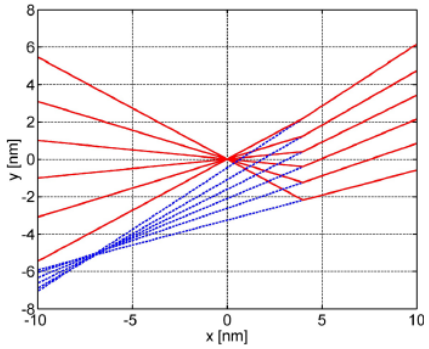

Fig. 11

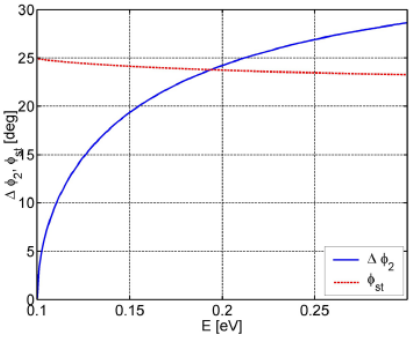

Fig. 12

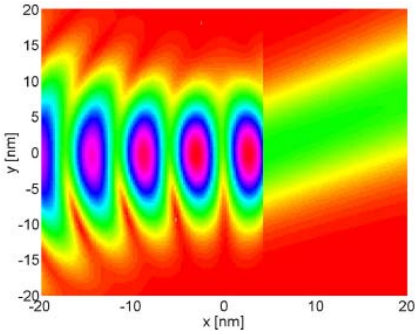

Fig. 13

These results, which suggest a new manipulation mechanism of ballistic electrons, were published in an ISI journal [P2] and were presented at an international conference [C1].

The propagation of electrons in type II heterostructures involves a correlation between the wavefunctions the conduction and valence bands, ψ_c and ψ_v, the total wavefunction having (up to a phase factor) the form $\psi^T = (\psi_c, \psi_v) = (1, \beta)$, where $\beta = \hbar P k/(E - E_v)$, with $k = [(E - E_c)(E - E_v)]^{1/2}/\hbar P$ the wave-number, P a measure of the correlation between the conduction and valence bands and $E_{c,v}$ the edges of this bands [8]. This wavefunction is similar to the Jones vector $J^T = (E_x, E_y)$, where $E_{x,y}$ are the components on the x,y axes of the electric field that propagates along the z direction [3]. In particular, the wavefunction in type II heterostructures is identical to the Jones vector of light polarized at an angle θ with respect to the x axis, if $\tan\theta = \beta$. The correlation between the electron energy E and the polarization angle θ of light is represented in Fig. 14 with solid line for InAs, the change of this angle at the InAs/AlSb interface, $\Delta\theta$, being represented with dotted line; the interface is similar to a device that rotates the polarization angle of light.

Regarding activity 1.3, we have shown that the electronic equivalent of the optical metamaterial, with dielectric constants $\varepsilon < 0$, $\mu < 0$, is a periodic medium consisting of layers denoted by 1 and 2, with widths $d = d_1 = d_2$, effective masses $m_1 > 0$, $m_2 < 0$ and potential energies $E - V_1 < 0$, $E - V_2 > 0$, surrounded by layers with $m_{in}, m_{out} > 0$, $E > V_{in}, V_{out}$. In this metamaterial regime, the transmission T through a structure with N periods is significant, even if the wavenumbers $k_i = [2m_i(E - V_i)]^{1/2}/\hbar$, i = 1,2, in both layers are imaginary, as can be seen from Fig. 15 for $m_1 = 0.04m_0$, $V_1 = 0.4$ eV, $m_2 = -0.02m_0$, V_2=0, $m_{in} = m_{out} = 0.03m_0$, $V_{in} = V_{out} = 0$, and N = 10, d = 2 nm (solid line), N = 10, d = 3 nm (dotted line) and N = 5, d = 2 nm (gray line). This result generalizes the class of nanostructures similar to metamaterials in optics [9], with specific propagation characteristics.

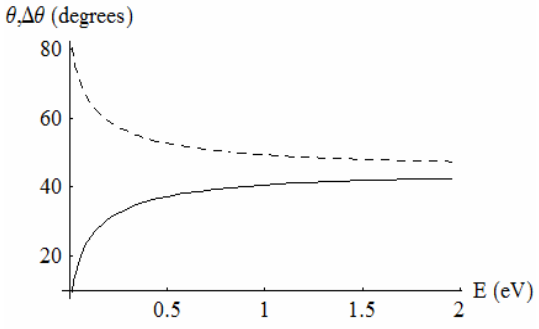

Fig. 14

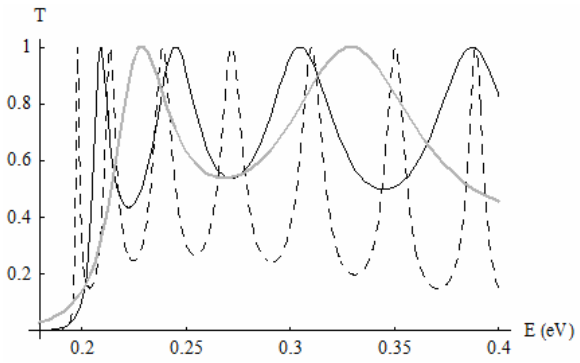

Fig. 15

The important parameters in high-frequency electronic circuits are the transfer/traversal times through nanostructures. Therefore, we have studied the dependence on the electron energy in the metamaterial

regime of the delay time $\tau_{ph} = \hbar[\partial \mathrm{Arg}(t)/\partial E]$, relevant for quasi-monoenergetic electron pulses, and of the traversal time $\tau_{tr} = \int dx/v_g(x)$, relevant for monoenergetic electron beams; $v_g(x)$ is the group velocity of electrons propagating along the *x* direction. For the situations in Fig. 15, these dependences are represented with the same line type in Fig. 16 and, respectively, Fig. 17, the times being normalized to the traversal time of a structure of width $L = N(d_1 + d_2) + d_1$ in the absence of the periodic medium, $\tau_0 = Lm_{in}/\hbar k_{in}$. It can be observed that there are energy ranges in which $\tau_{ph} < \tau_0$, the periodic structure accelerating the electron transport, but in all cases (at least in the example considered here) $\tau_{tr} > \tau_0$.

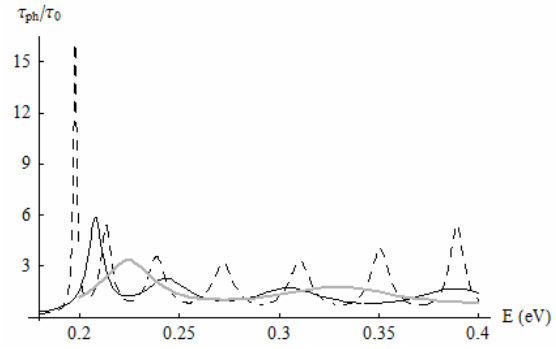

Fig. 16

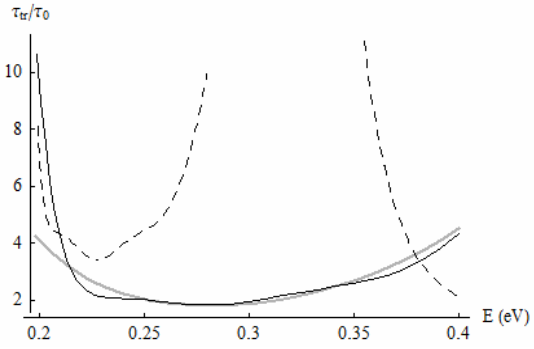

Fig. 17

These results were published in an ISI journal (publication [P3]) and presented at an international conference [C2].

Regarding activity 1.4, we showed that the propagation of the polarized states of light, represented by the Jones vector $J^T = (E_x, E_y)$, is analogous to electron transport through nanostructures in the presence of the Rashba effect [10]. The Rashba effect is a spin-orbit coupling that separates the energetic states of electrons with spin up and down due to the local electric field, perpendicular to the interface of the heterojunction, and caused by the inversion asymmetry of the structure. In a bidimensional electron gas located in the plane (*x*,*y*), in the presence of the Rashba efect (or of the equivalent magnetic field $B = 2\alpha k / g\mu_B$) the Hamiltonian is $H_{2D} = \hbar^2 k^2/2m + \alpha(k_y\sigma_x - k_x\sigma_y)$, where α is the Rashba coefficient, $\sigma_{x,y}$ are the Pauli matrices and $k_{x,y}$ are the components of the electron wavevector ***k*** along the directions *x*,*y*. The eigenfunctions of the electrons with spins up and down are given by (up to a phase factor) $\psi_+^T = (\cos(\phi/2), -\sin(\phi/2))$, $\psi_-^T = (\sin(\phi/2), \cos(\phi/2))$ with $\phi = \arctan(k_y/k_x)$, and are similar to the perpendicular Jones vectors of light linearly polarized at the angles $-\phi/2$ and $\pi/2 - \phi/2$ with respect to the *x* axis, or of light circularly polarized left/right [3]. An interesting application of this analogy is electron transport through an interface between a region in which the Rashba effect is absent and a region in which this effect is present. At normal incidence, the spins of incident electrons suffer a precession, as in the case of the optical Faraday effect, whereas at oblique incidence an electron beam splits in two beams with spins oriented perpendicular to the wavevectors of the two beams.

This phenomenon is analogous to the double refraction encountered in optics in uniaxial crystals, with ordinary and extraordinary refractive indices n_e and n_o. The Rashba effect is difficult to be observed in bidimensional electron gases because the electrons are not monoenergetic, are not incident on the interface at the same angle, their spin cannot be controlled precisely and, often, the Rashba effect is accompanied by other phenomena such as the Dresselhaus effect [11], which contributes to the electron Hamiltonian with the term $\beta(k_x\sigma_x - k_y\sigma_y)$. The analogy with classical optics can determine which of these factors limit the observation of the Rashba effect. An interesting result is that, if the Dresselhaus coefficient becomes $\beta = \alpha$, the wavefunction is independent of the electron momentum, which enhances the probability of observing the Rashba effect.

A qualitative electron-electromagnetic field analogy in the case of the Rashba effect can be found, for example, imposing the requirement that, for a crystal with given n_0 and n_e, the optical incidence angle δ_1 is chosen such that the propagation angle of the ordinary wave, δ_o, is equal to the propagation angle of

electrons with spin up or down in AlGaN/GaN in the presence of the Rashba effect, the propagation angle of the extraordinary wave, δ_e, being found from the Snell law. In Fig. 18 we have presented with black or gray lines, as a function of α normalized at $\alpha_0 = \hbar\sqrt{2e/m_0}$, the solutions found for the optical propagation angles corresponding to electrons with energy E = 0.25 eV incident at 15° on the Rashba medium with spin down or up, respectively, for n_0 = 1.67 and n_e = 1.55. Similar dependences, on electron energies are represented in Fig. 19, for $\alpha = \alpha_0$.

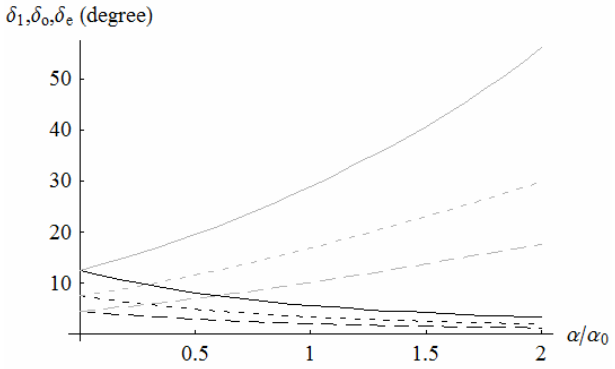

Fig. 18

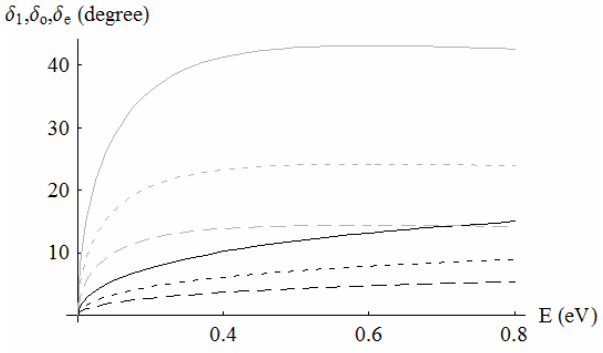

Fig. 19

In the presence of both Rashba and Dreselhaus effects, when $\beta = \alpha$, the optical analog of the electron gas is a uniaxial crystal with the optical axes oblique to the interface, at an angle χ. By imposing the condition of equality between the propagation and reflection angles of electrons with spin down and the optical extraordinary wave, the dependence of the optical axes tilt on the energy of electrons with spin down incident at an angle of 15° is illustrated in Fig. 20 for $\alpha = \beta = 0.05\alpha_0$ (solid black line), $0.07\alpha_0$ (dotted black line), $0.1\alpha_0$ (dashed black line), $0.15\alpha_0$ (gray solid line) si $0.2\alpha_0$ (gray dotted line). For other conditions, for example, equality of electron and optical propagation angles for χ = 20°, the incidence angle on the uniaxial crystal varies with the electron energy as shown in Figure 21.

The results obtained on the analogy between the electromagnetic fields and electrons in the presence of spin-orbit interaction were published in [P6].

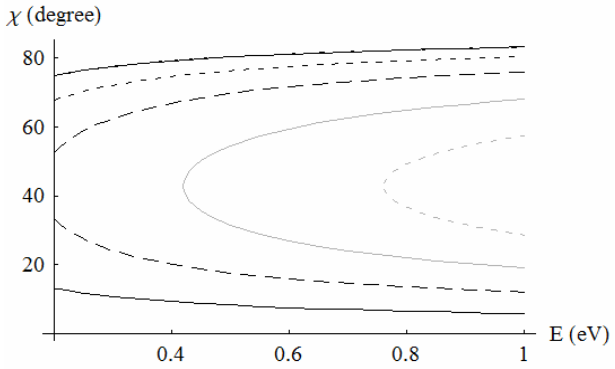

Fig. 20

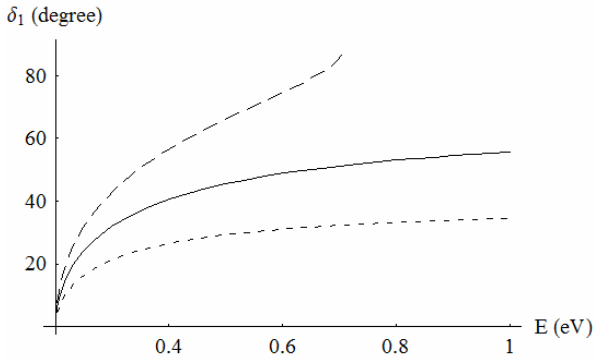

Fig. 21

Analogies between Dirac ballistic electrons and the electromagnetic field in gyrotropic and electro-optic, and complex conjugate media and in photonic crystals with Dirac points

These analogies encompass the project activities 4.2 (Design of structures in which the components of the electromagnetic field propagate similarly to electric charges in graphene devices), 4.3 (Effects of light polarization on the analogies between photonic crystals with Dirac points and graphene), and 4.4 (Effects of different boundary conditions on the analogy between the electromagnetic field and graphene). We have found that activity 4.4 cannot be treated independently from 4.2 and 4.3, so that the investigation was focused on two subjects: analogy electromagnetic field-graphene (which encompasses 4.2 and 4.4) and analogy photonic crystals with Dirac points-graphene (which encompasses 4.3 and 4.4).

Regarding the analogy electromagnetic field-graphene, we have shown that the propagation of electric charges in graphene, characterized by chirality, is similar to light propagation through gyrotropic and electro-optic media, and through complex conjugate media. In particular, the Dirac equation for the spinorial wavefunction in graphene, $\psi^T = (\psi_1, \psi_2)$, and the equation describing the propagation of polarized states of light with wavevector $\boldsymbol{\alpha}$ through a medium with gyrotropic coefficient γ and electro-optic coefficient β are similar [12]:

$$\frac{(E-V)}{\hbar v_F}\begin{pmatrix}\psi_1\\ \psi_2\end{pmatrix} = \begin{pmatrix}0 & k_x - ik_y\\ k_x + ik_y & 0\end{pmatrix}\begin{pmatrix}\psi_1\\ \psi_2\end{pmatrix}, \qquad (\alpha^2/k_0^2 - \varepsilon)\begin{pmatrix}E_x\\ E_y\end{pmatrix} = \begin{pmatrix}0 & \beta - i\gamma\\ \beta + i\gamma & 0\end{pmatrix}\begin{pmatrix}E_x\\ E_y\end{pmatrix}, \qquad (17)$$

where $k_0 = \omega/c$.

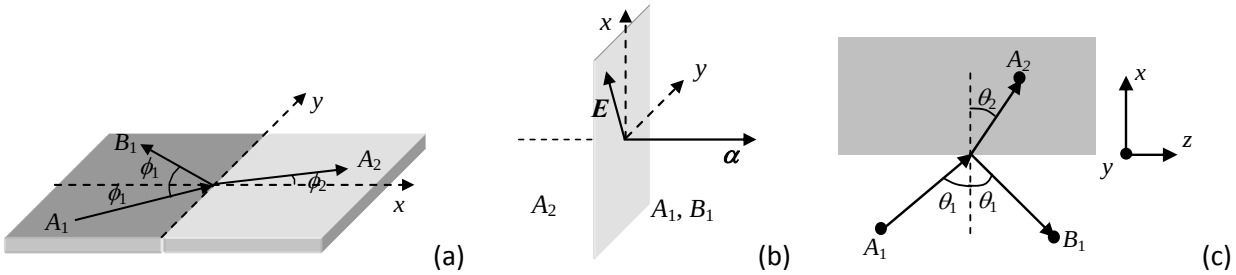

Fig. 22

Thus, the transmission coefficient of electrons with Fermi velocity v_F at an interface between two media with different potentials V in graphene (Fig. 22a), t_{gr}, and the ratio of the amplitudes of the independent, elliptical polarization states of light, t_{pol}, are similar, i.e. $t_{pol} = it_{gr}$, if the variation of light polarization $\Delta\theta = \arctan(\gamma/\beta)$ at an interface between media 2 (air) and 1 ($Cd_{0.5}Mn_{0.5}Te$), as in Fig. 22b, is appropriately correlated with the incidence angle of electrons in graphene. The dependence of $\Delta\theta$ on ϕ_1 and, respectively, that of the ratio between the magnetic field (which determines γ) and the electric field (which determines β) on ϕ_1 are illustrated in Fig. 23, for the range of incidence angles for which such a quantitative analogy exists.

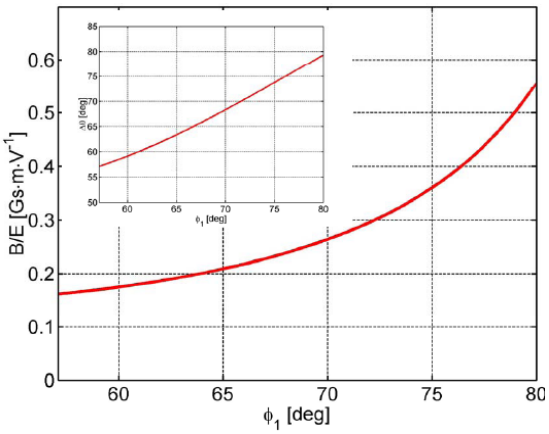

Fig. 23

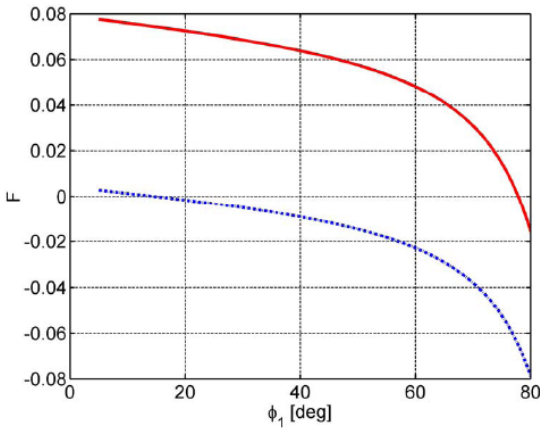

Fig. 24

In the second case, the propagation of electrons through an interface in graphene is put into correspondence with light propagation through an interface between air and a complex conjugate medium (Fig. 22c), in which the relative dielectric constants are complex: $\varepsilon_r = m(a + ib)$, $\mu_r = a - ib$, but the refractive index $n = (\varepsilon_r \mu_r)^{1/2} = [m(a^2 + b^2)]^{1/2}$ is real [13]. For m = 1, a = 1.5 and b = -0.05, the optical transmission coefficient, t_{ccm}, is identical to t_{gr} if $F = [\cos\phi_1(\sin\phi_1 - \sin\phi_2)]/[1 + \cos(\phi_1 + \phi_2)] - \mathrm{Im}[t_{ccm}] = 0$. This condition can be satisfied on a wide range of light incidence angles, 6° < θ_1 < 42°, the solid red and dotted blue lines in Fig. 24 corresponding to the optical incidence angles 10° and 40°.

The obtained results, which confirm the fact that the electron chirality in graphene can be mimicked in classical optical systems, were published in an ISI journal [P4], presented at an international conference [C3] and at an international Heraeus seminar (two contributions, [C4] and [C5], the first one being invited).

Regarding the analogy photonic crystals with Dirac points-graphene, the study started from the fact that Dirac points in photonic crystals exist only for TE polarization and not for TM polarized light. For TE light the Dirac equation can be written as

$$\begin{pmatrix} 0 & v_D(k_x - ik_y) \\ v_D(k_x + ik_y) & 0 \end{pmatrix} \begin{pmatrix} \Psi_1 \\ \Psi_2 \end{pmatrix} = 2(\omega - \omega_D) \begin{pmatrix} \Psi_1 \\ \Psi_2 \end{pmatrix} \tag{18}$$

(similar to that in graphene) and is satisfied by the degenerate Bloch states $\Psi_{1,2}$ in the corners of the first Brillouin zone, with v_D the light velocity in the homogeneous medium and ω_D the frequency at the Dirac point. The graphene-photonic crystals with Dirac point analogy was investigated from the point of view of the linear dispersion relation for light, as in graphene, in photonic crystals surrounded by regions in which light satisfies the Maxwell equation, respectively regions in which electrons satisfy the Schrödinger equation. This problem has been treated independently in optics [14] and in graphene devices [15], the results suggesting that the transition between the Maxwell-Dirac-Maxwell equations for photons and Schrödinger-Dirac-Schrödinger for electrons lead to a dramatic decrease of transmission compared to the situation in which no such transformation of the governing photon/electron equation occurs. The advantage of correlating the results in optics and graphene is that one can fabricate a photonic crystal that simulates the propagation of electrons in contacted graphene. This problem is important since the influence of contacts, in which electrons satisfy a Schrödinger equation, on the performances of graphene devices is not fully understood.

The graphene-photonic crystal analogies are not unique since they depend on the wavefunction continuity conditions at the contact/graphene interface. For instance, the dependence of electron transmission on energy and the incidence angle vary as a function of the continuity conditions, but these conditions are not known and there is no motive to favor a certain condition. Thus, fabricating a photonic crystal and studying its transmission as a function of the incidence angle could solve the problem of finding the proper boundary conditions at the interface between graphene and metallic or semiconducting contacts; the aim is to increase the transmission as much as possible. For example, in Fig. 25 (a) and (b) we have represented the transmission dependence on the effective masses, m_1 and m_3, of electrons in the contacts, for two different boundary conditions. As can be seen, optimum transmission can be achieved for identical or different contacts, depending on the boundary conditions.

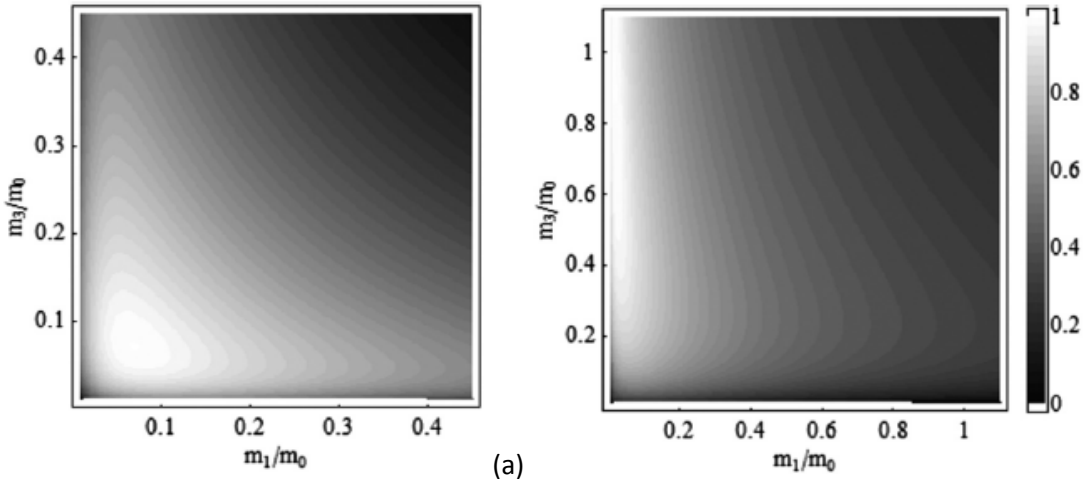

Fig. 25 (a) (b)

Development of algorithms for simulating inhomogeneous and disordered nanostructures

Besides studying the analogies between ballistic electrons and the electromagnetic field, we started to develop computational algorithms for simulating the electric transport in inhomogeneous and disordered nanostructures [16]. The aim is to find the configuration that is closest to an optical medium that amplifies or absorbs electromagnetic radiation.

The major difficulty in the treatment of charge transport in nanostructures, seen as open quantum systems, is to determine the wavefunctions for a sufficiently wide energy range, necessary to solve the coupled Schrödinger and Poisson equations. The R matrix formalism could solve this problem. It involves two computing steps: (i) the calculation of energy eigenvalues for the considered physical system, with fixed boundary conditions, and (ii) the calculation of the wavefunction and the transmission coefficient at each energy with a much lower computational cost.

In this respect, in the *R* matrix formalism, the physical system is divided in an internal region Ω_0 ("scattering region", in which the actual interactions take place) and an external region Ω_s, corresponding to the contacts (semi-infinite and translational invariant, with a confining potential that defines the transport channels). The geometry of the problem is described in Fig. 26. In this case, the wavefunction of an electron incident in channel ν from contact *s* is

$$\psi(\boldsymbol{r} \in \Omega_S; E) \quad = L^{-1/2}[\exp(-ik_\nu z_S)\phi_\nu(\boldsymbol{r}_{\perp,s}) + \sum_{\nu'} S_{\nu\nu'}(E)\exp(ik_{\nu'} z_S)\phi_{\nu'}(\boldsymbol{r}_{\perp,s})] \tag{19}$$

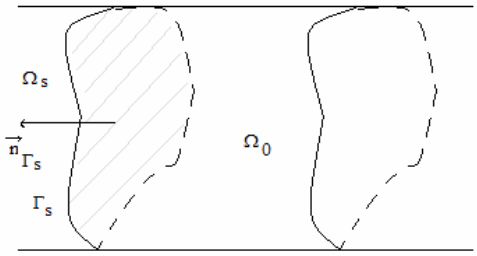

Fig. 26

the elements of the scattering matrix *S* being related to the transmission functions as $T_{\nu\nu'}(E) = | S_{\nu\nu'}(E) |^2$. In the scattering region the wavefunctions are solutions of the stationary Schrödinger equation in the self-consistent potential $W_{SC}(\boldsymbol{r})$, and are expressed in the complete system of the wavefunctions $\chi_l(\boldsymbol{r})$ of an auxiliary Wigner-Eisenbud problem with eigenenergies E_l. To find the matrix *S* it is necessary to determine first the function *R* defined as

$$R(\boldsymbol{r}, \boldsymbol{r}'; E) = -(\hbar^2/2m)\sum_l \chi_l(\boldsymbol{r})\chi_l^*(\boldsymbol{r}')/(E - E_l) \tag{20}$$

from which *S* is obtained as $S = -[I + (i/m)R\kappa][I - (i/m)R\kappa]^{-1}$, where *I* is the unit matrix, *R* is the matrix with elements determined by the *R* function and κ is a diagonal matrix with elements determined by the wavenumbers of the electrons incident in different channels.

To implement numerically the formalism of the *R* matrix we used an iterative self-consistent method to solve the system of coupled Schrödinger and Poisson equations, based on a linear mixing procedure for the self-consistent potential or on a Broyden type. Several sections of the developed numeric code were parallelized, which reduces drastically the computing time. The development of these algorithms allows the computing of transport characteristics of inhomogeneous structures. We intend to study geometrical and dopant/charge carrier concentration inhomogeneities in order to determine which configuration can be considered the closest to an optically active medium.

Results obtained in the 2013 stage of the project

In 2013 we have performed intensive simulations of electron transmission in inhomogeneous and disordered nanostructures based on the *R* matrix method. We have used the computation algorithms developed in the last part of 2012 and optimized them.

The objective of the 2013 stage was to establish an analogy with light propagation in active disordered media. Such an analogy was not studied up to now. For light, it was determined that the localization threshold in disordered structures depends on the homogeneous or inhomogeneous character of the distribution of scattering centers [17]. The spatial confinement of light favors the localization of

electromagnetic waves with certain wavelengths due to the dependence of the induced interference in structures with low dimensionality on the light wavelength [18]. In addition, if the optical medium is active, i.e. absorber or amplifier, the localization threshold of light depends also on the absorption coefficient, which prevents photon localization since it impedes the interference of scattered light, or on the gain coefficient, which favors the localization by enhancing light amplification [17,18].

These considerations put the light-electron analogies in disordered media in a new perspective. In optically active media, the intensity of light increases or decreases with the propagation distance, depending on the absorber or amplifier character of the medium. On the other hand, for electrons the current (considered usually similar to the optical intensity) is constant throughout the conductor. Thus, a spatial inhomogeneity for electron propagation can only be a conductor in which the concentration of free electrons, the transverse dimension of the conductor or the concentration of the scattering centers vary in space.

To define the configuration of an inhomogeneous nanostructure analogous to an active optical medium, which is the objective of the activity 1.1, we took into account also practical considerations. The case when the transverse dimension of the conductor is not constant has no practical utility, so that this situation was not investigated. On the other hand, a spatially varying electron concentration leads to the appearance of an internal electric field, with no equivalent in optics, except media in which the refractive index varies spatially; such media, especially when disordered, are difficult to fabricate. Therefore, we have considered that a spatially varying scattering of electrons is more likely to correspond to a disordered optical active medium, and have chosen this case for numerical investigations. In addition, this situation is relevant in practical applications since the disorder/distribution of scattering centers can vary gradually in the fabrication process of nanostructures.

The first simulations of this configuration of interest focused on a homogeneous bidimensional nanostructure, with a disordered distribution of the scattering centers (impurities). The study of such a structure corresponds to the activity 1.2. We have computed the charge transport, in particular the transmission, in these nanostructures with either attractive or repulsive impurities modeled as distributed Gaussian potentials

$$V(\boldsymbol{r}) = \sum_{\alpha} V_0 \exp\left(-\frac{(\boldsymbol{r}_\alpha - \boldsymbol{R}_\alpha)^2}{2\sigma^2} \right) \tag{21}$$

where $\boldsymbol{r}_\alpha$ are the centers of a quadratic grid and $\boldsymbol{R}_\alpha$ are chosen arbitrarily in the scattering region, as a function of an order parameter. The scattering potential V_0 is –1 eV for attractive impurities and 1 eV for repulsive ones and the standard deviation σ = 1 nm was considered the same for all scattering centers. The order parameter η defines the shift of the scattering centers with respect to the 10×10 quadratic grid: $\boldsymbol{R}_\alpha = \boldsymbol{R}_\alpha^0 + \delta\boldsymbol{R}$ cu $\delta\boldsymbol{R} = L(1-\eta)r_1\hat{\boldsymbol{x}} + L(1-\eta)r_2\hat{\boldsymbol{y}}$, where *L* = 80 nm is the side of the scattering center and $r_{1,2}$ are random numbers between 0 and 1. For η = 1 the system is ordered, while η = 0 corresponds to complete disorder. We have assumed a quadratic scattering region surrounded by ideal contacts, the electron effective mass being chosen as that in GaAs: $m = 0.065m_0$.

The parameter of interest is the total electron transmission between source and drain contacts, T_{SD}, calculated as a sum over all open channels (the normalized conductance value); as such, this parameter can be larger than unity. The total transmission was represented in the figures below after averaging over 100 ensembles with distinct disorder.

Figure 27 illustrates the transmission for attractive scattering centers for η = 1.000, 0.994, 0.990, 0.986, 0.980, 0.970, 0.960, 0.940, 0.900, and 0.000, the respective curves varying from top to bottom in region A. In the inset of Fig. 27 we have represented the transmission for high values of the order parameter: 1.000, 0.998, 0.996, 0.994, 0.992, 0.990. It can be seen that the sharp maxima of transmission tend to flatten as the order decreases, while the forbidden region, located between 0.06 and 0.1 eV for a completely ordered system, disappears as η decreases to values of 0.97-0.98. This forbidden region is caused by a superlattice effect. This region in the case of attractive impurities is evidenced also by the plateau in the integral over

the transmission coefficient, represented in Fig. 28. This figure suggests the existence of a phase transition for η in the range [0.97,0.98].

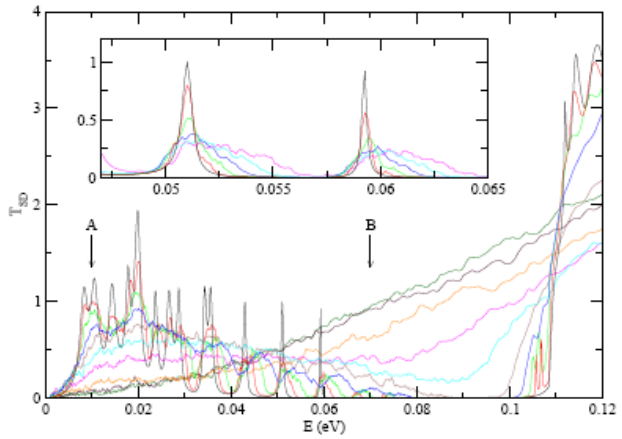

Fig. 27

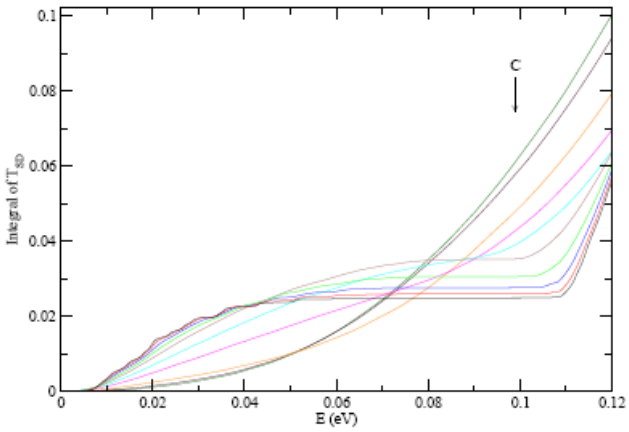

Fig. 28

The energy dependence of the source-drain transmission for repulsive scattering centers is illustrated in Fig. 29. The curves decrease in amplitude for η values of 1.000, 0.990, 0.985, 0.980, 0.970, 0.000, 0.920. As in the case of attractive impurities, the maxima flatten as the disorder increases, and the threshold energy value at which the transmission is significant decreases as η takes smaller values. This effect can be explained by a decrease of the backscattering efficiency of the ordered array of repulsive impurities.

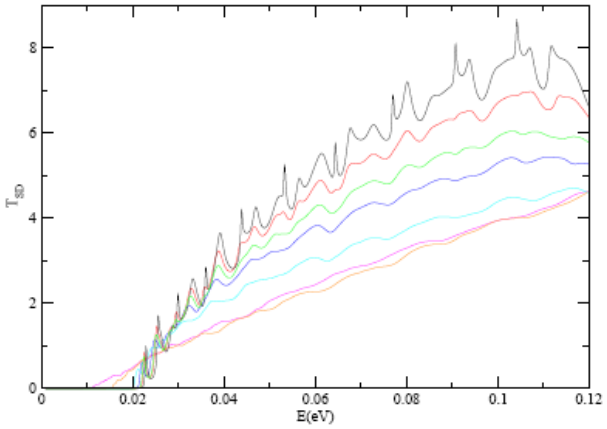

Fig. 29

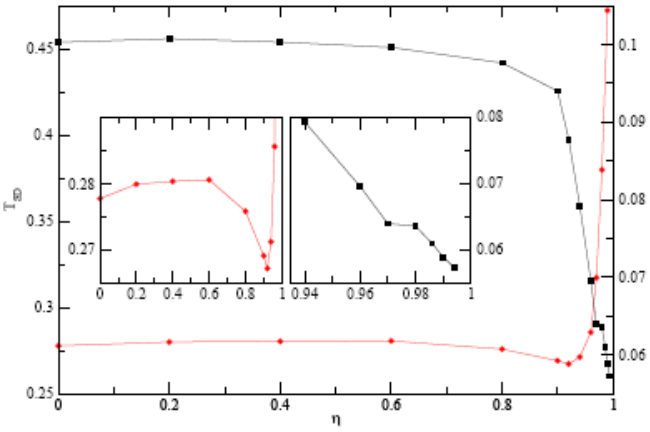

Fig. 30

The significant difference between the effects of the attractive and repulsive scattering centers is evidenced also by the energy dependence of the integrated total transmission, represented in Fig. 30 with black and, respectively, red lines. From this figure it can be seen that the integrated transmission decreases sharply at a certain η value for repulsive impurities, and increases rapidly for the attractive ones. The cause of this phenomenon is under investigation. The numerical simulations show that the value and the energy dependence of the transmission coefficient can be modified by the presence (intentional or not) of impurities of a certain type: attractive or repulsive. These results have been presented at an international conference [C6].

It should be emphasized that the transmission in disordered conductors has a far more complex behavior than light scattering, since there are two types of scattering centers in this case (attractive or repulsive) and the transport of charge carriers is different in these cases. The two types of impurities have no optical analog. Moreover, the two types of active media in optics (absorber or amplifier) cannot be put in direct correspondence with the attractive or repulsive impurities in the case of electrons since in the last case not only the amplitude of the wavefunction changes, but also the interaction.

A study of the influence of the two types of scattering centers on electron transmission in inhomogeneous and strongly confined nanostructures is presented in Fig. 31 and, respectively, Fig. 32. the bidimensional

structure has a width W = 40 nm and a length L = 160 nm, the N = 100 impurities being placed in an ordered manner (in the nodes of a grid with equal distance along the transverse y direction and not equal distances along the longitudinal x direction) but distributed spatially according to a polynomial law. More exactly, the impurity concentration was chosen to vary as

$$n_m(x) = n_{0m} x^m, \qquad \int_0^L n_m(x)dx = N \tag{22}$$

In Fig. 31 and 32 we have presented the total source-drain transmission for m = 1, 1.5, 2, 2.5 and 3, the black line indicating the transmission value in the absence of scattering centers. The value m = 1 corresponds to a homogeneous and ordered distribution. Surprisingly, at least at first glance, is that the transmission behaves similarly for attractive and repulsive impurities. The step-like variation of transmission for both attractive and repulsive scattering centers follows the transmission of an ideal conductor (with no impurities), the energy thresholds being in agreement with the results in Figs. 27 and 29. In addition, it can be seen that the inhomogeneous distribution of impurities has a similar effect on transmission as the disorder in an array of homogeneously distributed scattering centers. In particular, the step-like transmission shape is no longer evident as the inhomogeneity increases and the transmission value decreases, the decrease being more visible for attractive scattering centers.

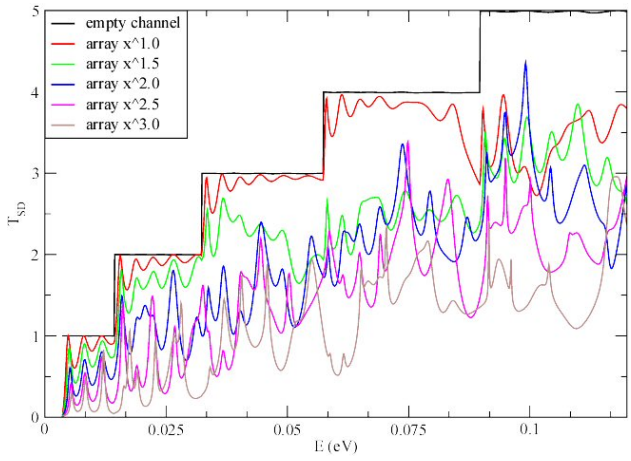

Fig. 31

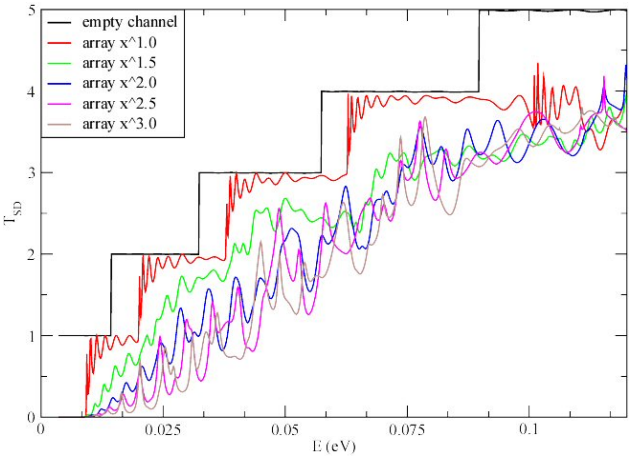

Fig. 32

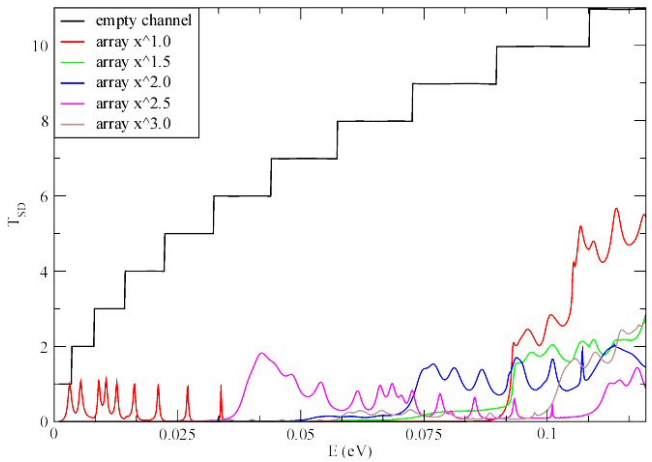

Fig. 33

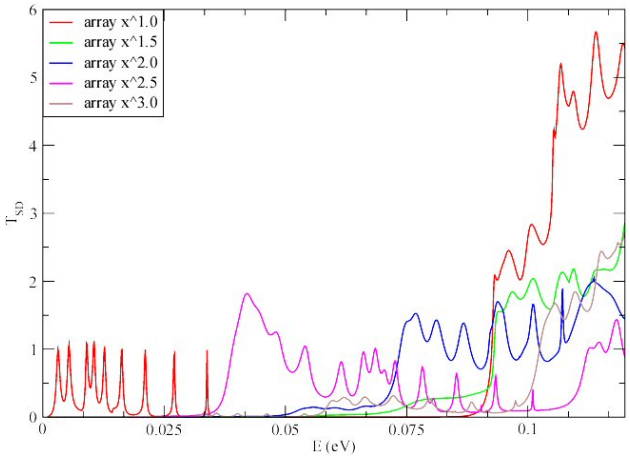

Fig. 34

The simulation results in Figs. 31 and 32 have not revealed significant differences between the effects of attractive and repulsive scattering centers because the spatial confinement was too strong. Therefore, we have studied a wider bidimensional conductor with W = L = 80 nm, in which we have distributed the N = 100 impurities in an ordered manner according to the polynomial law (22). The results for attractive scattering centers are presented in Fig. 33, a detail of this figure being shown in Fig. 34.

A comparison with Fig. 27 leads to the following conclusions (i) for *m* small (moderately inhomogeneous) the transmission coefficient behaves similarly to the case of a homogeneous distribution of ordered impurities, (ii) as the parameter *m* increases (the inhomogeneity increases) the forbidden region, in which the transmission coefficient T_{SD} vanishes shift toward smaller energies and the value of T_{SD} decreases (in the disordered system the forbidden region is not shifted), (iii) the oscillatory behavior of the transmission coefficient is apparent for all *m* values, being caused by the interference of the wavefunction in the ordered array of scattering centers. On the other hand, the global behavior of the transmission is similar to the case of a disordered homogeneous system. In all situations, the value of T_{SD} is much smaller than in a nanoscale conductor with no scattering centers (see the black line in Fig. 33).

The energy dependence of the transmission coefficient for repulsive impurities positioned in an ordered but inhomogeneous manner is illustrated in Fig. 35, while a detail of this figure is shown in Fig. 36. In this case the value of T_{SD} is higher than for attractive impurities, in agreement with the simulation results for the disordered case. Again, the general behavior for *m* small is similar to the case of the disordered and homogeneous distribution of repulsive scattering centers, significant values of transmission appearing at higher energies as *m* increases. The last observation does not agree with the T_{SD} behavior in homogeneous conductors. In addition, the energy dependence of the transmission coefficient is almost identical for *m* > 2, except for the oscillations in T_{SD} (due to the interferences of the wavefunction in the ordered structure), which tend to become irregular.

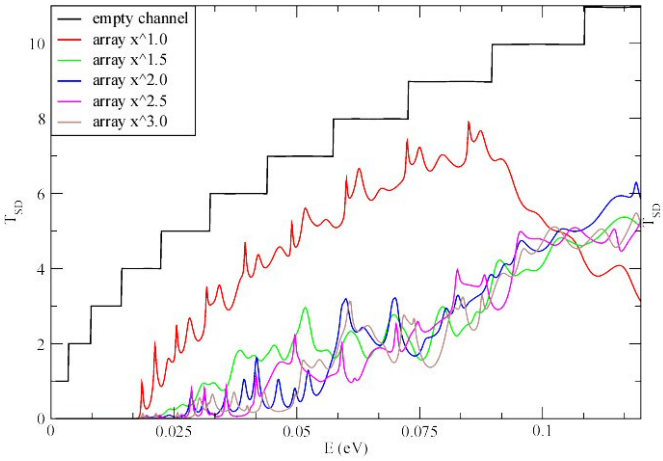

Fig. 35

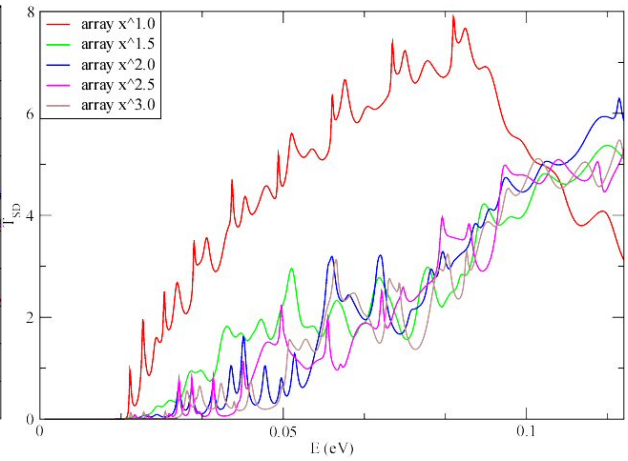

Fig. 36

So, unlike for attractive scattering centers, the non-homogeneity of repulsive impurities has a much smaller influence on electron transport. This result has a practical importance, since it implies that the fabrication tolerances of nanometer-scale device can be relaxed if repulsive impurities are introduced. The numerical simulations obtained in 203 were published in an ISI journal [P7].

Results obtained in the 2014 stage of the project

The 2014 stage of the project focused on the fabrication of inhomogeneous nanowires, in which the density of carriers/scattering centers is variable and controlled, and on the morphological characterization of these structures. This activity was time-consuming such that, in order to find the optimum conditions in which the inhomogeneity of charge carriers has observable effects, we continued to perform numerical simulations for nanowires with variable concentrations of charge carriers along the longitudinal direction (along the wire axis). In the following we detail the results obtained in optimizing the profile of the inhomogeneous distribution of scattering centers as well as in fabricating the nanowires.

Optimization of the effect of inhomogeneous distribution of scattering centers on ballistic transport

An inhomogeneous distribution of scattering centers can enhance the thermal and/or transport characteristics of some devices. For example, the Seebeck coefficient and the electrical conductivity in polycrystalline materials can simultaneously increase [19], or the luminosity of polymeric LED can increase

[20]. The modeling of such a distribution of scattering centers has been done up to now for diffusive transport only [21-23], quantum effects being considered only in nanosystems with a spatially inhomogeneous cross-section [24].

In order to study the effect of inhomogeneous scattering centers on charge transport, we calculated the transmission coefficient of ballistic carriers using the R matrix formalism [16], presented above. In particular, we simulated an ordered distribution of scattering centers/impurities, in which the gradient of the scattering center concentration is finite. Thus, we could focus exclusively on the effect of inhomogeneity of impurities on the transmission coefficient. In the geometry of the problem, shown in Fig. 37, the scattering centers (represented by points) are modeled by Gaussian potentials, in which the spatial distribution along the transverse *y* direction is homogeneous but along the longitudinal *x* direction varies as $x \propto n^p$, where *n* labels the impurity column along *x*.

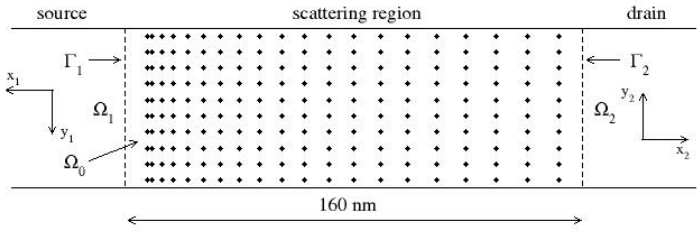

Fig. 37

The charge carriers incident from the left contact (source) interact with scattering centers in the central region and are collected by the right contact (drain), the interaction being described by the time-independent Schrödinger equation, in which the one-particle Hamiltonian in the effective mass approximation is

$$H = -\frac{\hbar^2}{2m}\Delta + W(\boldsymbol{r}), \qquad W(\boldsymbol{r}) = \Sigma_\alpha V_0 \exp\left(-\frac{(\boldsymbol{r}-\boldsymbol{r}_\alpha)^2}{2\sigma^2}\right) \tag{23}$$

where *m* is the effective mass of carriers, $\boldsymbol{r} = (x, y)$ is the position vector, $\boldsymbol{r}_\alpha$ denotes the position of the impurity center with Gaussian potential and standard deviation *σ*. We modeled the effect of both attractive and repulsive impurities by choosing V_0 = −1 eV and, respectively, 1 eV, in both cases having σ = 1 nm.

As an example, we studied a bidimensional electron gas in GaAs in which m = 0.0655 m_0, the scattering region, with length of 160 nm and width of 80 nm, containing 20 × 10 scattering centers. Considering ideal contacts, we simulated scattering on attractive and repulsive impurities with *p* = 1, 1.05, 1.1 and 1.5. The first case corresponds to a periodic arrangement of impurities.

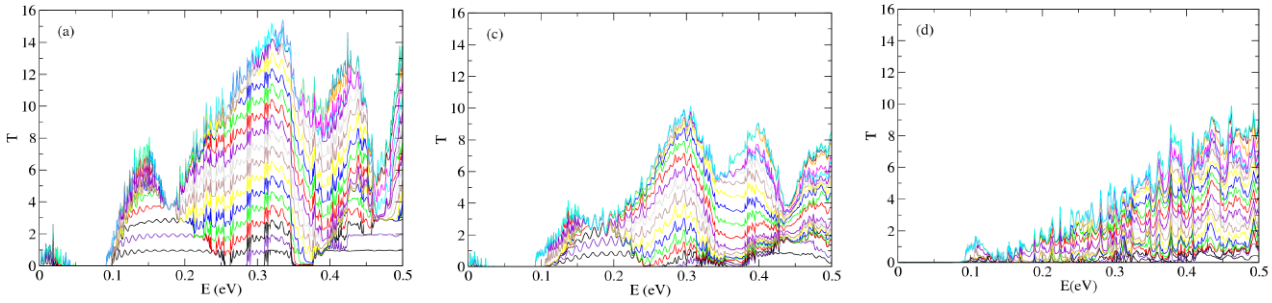

Fig. 38 (a) (b) (c)

In Figs. 38(a)-(c) we represented the energy dependence of the source-drain transmission coefficient *T* for *p* = 1, 1.1 and, respectively, *p* = 1.5, for attractive impurities and for an increasing number of channels. For *p* = 1 (Fig. 38(a)) a succession of allowed and forbidden energy bands form as a result of the superlattice effect in periodic structures. However, remnants of energy bands can still be observed, at low energy, up to *p* = 1.1. The maxima of the transmission coefficient are wide in the allowed bands and have a triangular shape because the electrons in different channels/with different energies *E* feel a different potential energy distribution, the widths and heights of the periodic Gaussian potential wells depending on *E*. Between 0.04 eV and 0.9 eV a forbidden energy band appears, in which *T* = 0. As the inhomogeneity (*p* value) increases,

the potential profile is no longer periodic and the maxima decrease in amplitude until, in sufficiently inhomogeneous structures, the transmission coefficient varies almost linearly with energy, as in the case of disordered systems [C6]. For attractive impurities the transmission range up to 0.04 eV vanishes for p = 1.5.

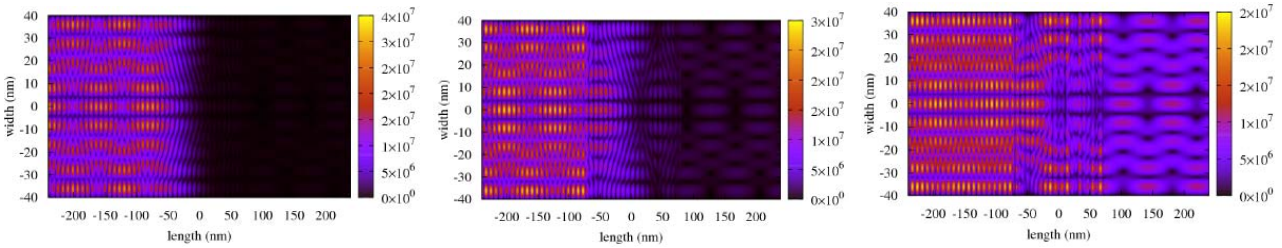

Fig. 39 (a) (b) (c)

Besides modifying the energy dependence of the transmission coefficient, the inhomogeneous distribution of attractive scattering centers leads to mode mixing in the scattering region, especially at high energies. Extensive simulations (see publication [P7]) showed that the probability distribution of carriers for a given channel depends non-uniformly on p: in general, for lower-order channels the electron wavefunction modulus maintains its form but decreases as p increases, while for higher-order channels both the shape and the probability distribution value changes with p, with no clear trend. For example, in Figs. 39(a)-(c) we have represented the variation with p (p = 1, 1.1 and, respectively, 1.5) of the wavefunction modulus throughout the whole structure (contacts and scattering region) for the 9th channel at E = 0.178 eV, energy for which T is minimum. Besides emphasizing the electron redistribution among the open channels, this figure shows the tendency of increasing as p increases of the probability at the outer edges of the scattering region, which suggests structures sensitive to surface effects, and thus appropriate for sensing applications.

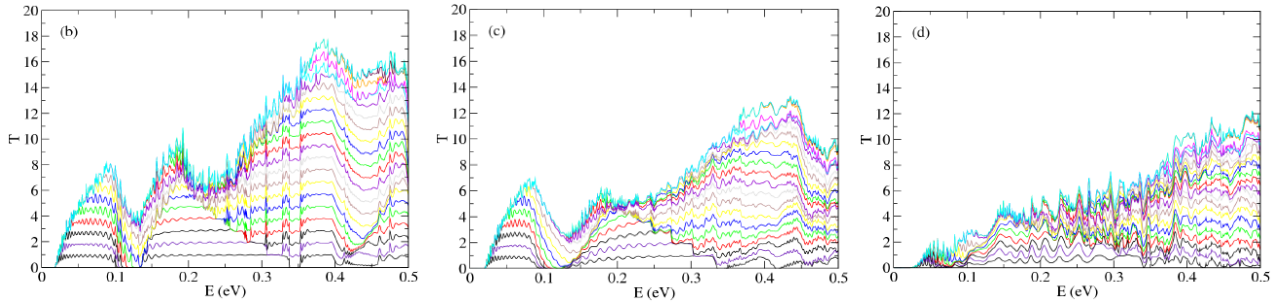

Fig. 40 (a) (b) (c)

A similar treatment of repulsive impurities show the same tendency of decreasing of transmission maxima as p increases and an almost linear dependence of T on energy for p = 1.5 (see Figs. 40(a)-(c) in which the energy dependence of T is represented for p = 1, 1.1 and, respectively, p = 1.5, for an increasing number of channels). Although for p = 1 we observe the same wide and triangular maxima, due to the structure periodicity, which disappear gradually for an increase in inhomogeneity of the impurity distribution, the maxima seem to be more robust than for attractive impurities, and can be observed at small energy even for p = 1.5. The transmission threshold, located at 0.02 eV for p = 1 and caused by the formation of a bandgap at lower energies, shifts to higher energies as p increases.

Again, different modes become mixed, the electrons being redistributed among the open channels, without identifying a particular behavior of the probability distribution and T with p. Simulations of the wavefunction modulus show that, in general, the transmission of lower-order channels increases with p, but the transmission value and the shape of the probability distribution for higher-order channels are less influenced by the p value than for attractive impurities. Unlike for scattering on attractive centers, in this case the wavefunction modulus is concentrated in the central region for certain channels, for example for the 9th channel at E = 0.134 eV (for which the total transmission is minimum). The behavior of the wavefunction in this case, represented in Figs. 41(a)-(c) for p = 1, 1.1 and, respectively, 1.5, suggests a decrease of sensitivity at surface effects

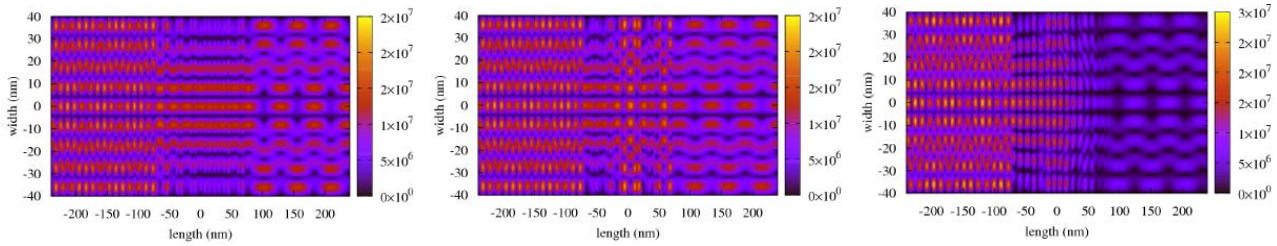

Fig. 41 (a) (b) (c)

The results of these simulations were published in the paper [P7] and were presented at an international conference [C7].

Fabrication of nanowires with inhomogeneous distribution of scattering centers

The numerical simulations above show that an inhomogeneous distribution of scattering centers, even an ordered one, affects the ballistic transport in a similar manner to a random distribution of impurities, this fact being observable even for propagation distances of only tens of nm. As such, the benefits of doping for electronic devices based on nanowires could be most clearly emphasized in segmented nanowires. To fulfill the objectives of this stage of the project, arrays of Ni nanowires (uniform at first, to calibrate the growth method, and segmented afterwards, of the type Ni/Cu) were grown electrochemically in the nanopores of an alumina template.

Nanostructured systems based on Ni and on its alloys are important for sensing applications due to their magnetic and catalytic properties, which are strongly dependent on composition, dimensions, shape and morphology of nanowires. The matrices of uniform or segmented Ni wires, including Ni/Cu wires, were produced by a template method. This method is commonly used to fabricate wires with controlled diameters [25-28]. The template was alumina, in which a matrix of nanopores was created by controlled anodization.

Fabrication of the alumina template

The template is fabricated on a substrate, which is a Si(111)/SiO_2 wafer (the width of the SiO_2 layer is 30 nm), cleaned by ultrasonication in a bath of organic solvents (benzene and acetone). The wafer is first covered with an Au film of 200 nm, deposited by DC cathodic pulverization. The Au film has the role of:

a) anodization barrier for the subsequent deposition of the Al film;

b) working electrode in the electrochemical anodization process, and during the subsequent electrochemical deposition of nanowires.

The third layer is Al (350 nm thick), also deposited by DC cathodic pulverization. The anodization of the Al film was performed in a home-made electrochemical cell for an optimum control of the temperature of the electrolytic bath. A three-electrode working configuration was used (consisting of the two working electrodes and a commercial reference electrode from saturated calomel – SCE). The anodization temperature must be kept around 3-5^{o}C, to avoid nanopore closure. The anodization electrolyte consists of a mixture of oxalic and phosphoric acids, the complete chemical reaction being:

$$2Al + 3H_2O \rightarrow Al_2O_3 + 3H_2 \quad (24)$$

The alumina membrane shows a high density of nanopores, with a typical morphology as that in the SEM image in Fig. 42.

The chrono-ampermetric curve recorded during the anodization process and presented in Fig. 43 reveals the three stages of the anodization process:

1) the formation of a thin Al_2O_3 layer at the cathode surface (Al film), associated to the initial sharp decrease of the current;

2) the equilibrium between the two competing processes: dissolution of the formed oxide in the region of intense electric field and continuation of the oxidation process, the competition between these processes leading to nanopore formation;

3) nanopore growth up to the Au electrode, which inhibits oxidation, and leads to a sharp increase of the current due to the electrolyte short-circuit.

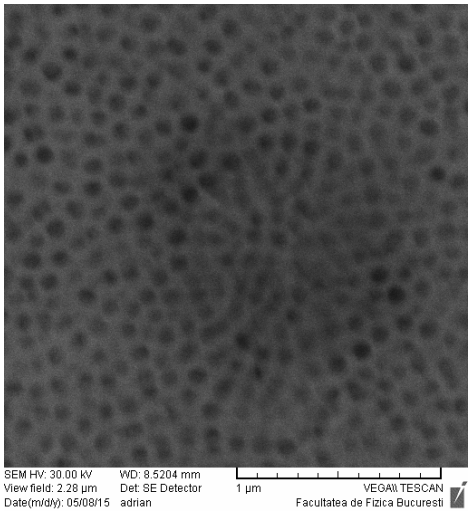

Fig. 42

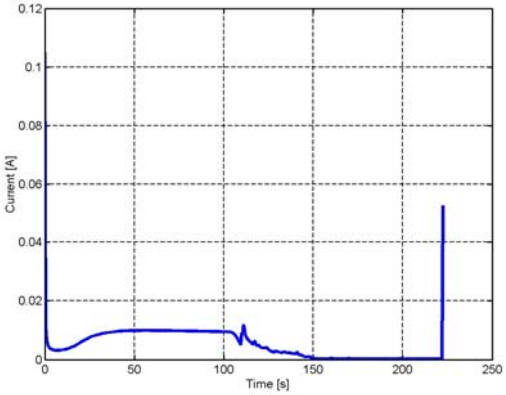

Fig. 43

Fabrication of the matrix of Ni nanowires

The Ni nanowires were grown in the pores of the alumina membrane by an electrochemical procedure. The electrochemical deposition has the advantages of low cost and possibility of achieving with not very sophisticated equipmets. Combined with the template method, the electrochemical deposition is very versatile, and can be used to grow wires from either metal or semiconductor materials. Homogeneous or segmented wires can be obtained by controlling specific growth parameters [29-31]. The Ni nanowires were obtained using as electrolyte a Watts bath containing 225 g/L of $NiSO_4 \cdot 6H_2O$ and 30 g/L of $NiCl_2 \cdot 6H_2O$. A VoltaLab potentiostat was used to control the electrochemical process via a computer, in the three-electrode configuration with an Au cathode, a platinum anode and a SCE reference electrode. The temperature was kept at 5^oC during the growth of Ni wires. Under these conditions the reaction at the cathode is:

$$Ni^{2+} + 2e^- \rightarrow Ni^0 \qquad (25)$$

A typical chrono-ampermetric curve recorded during the growth of wires inside the pores is shown in Fig. 44.

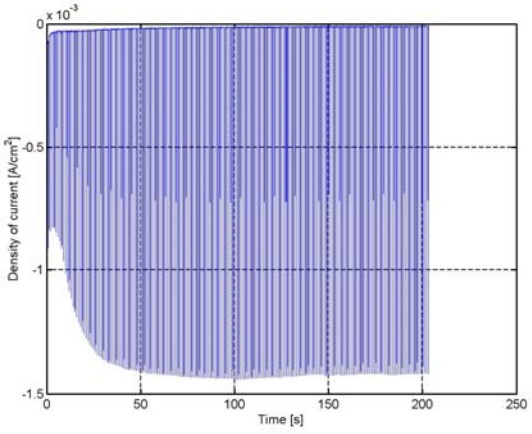

Fig. 44

After the pores are filled, the template membrane is dissolved in an alkaline solution of NaOH, so that the matrix of Ni wires remains exposed. Figures 45(a)-(c) present SEM images, with increasing magnification, of the nanowire matrix grown on a set of Au interdigitated electrodes. As can be observed from these figures, the nanowires grow only on the metallic surfaces/interdigitated electrodes.

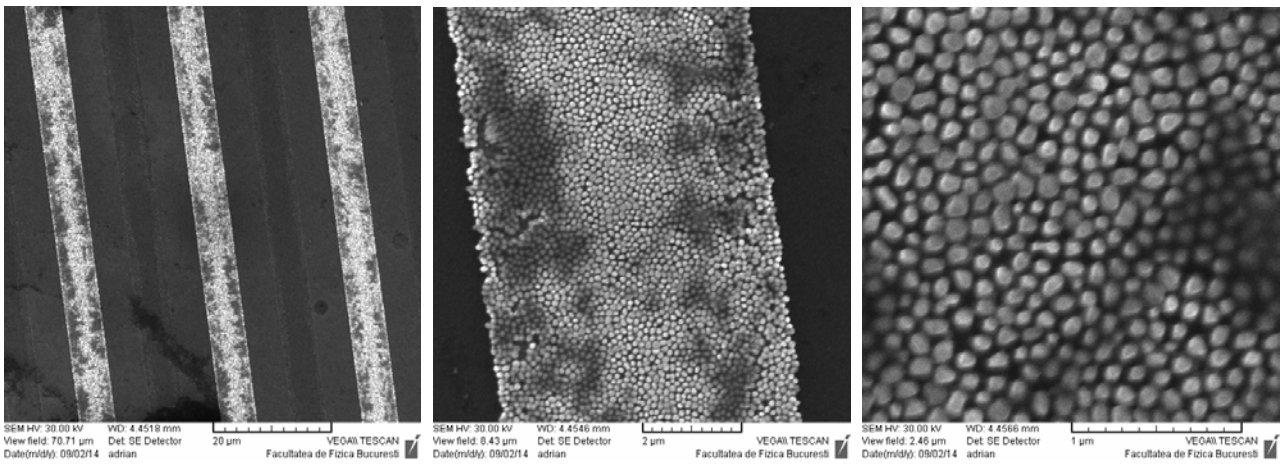

Fig. 45 (a) (b) (c)

This type of electrodes was then used as chemical sensor of glucose, with capacitive detection. The lock-in detection system is represented schematically in Fig. 46. This type of sensor has the advantage of an enhanced sensitivity due to the large surface/volume ratio.

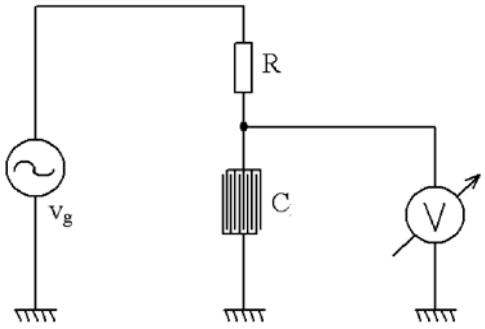

Fig. 46

The capacitive response was measured by impedance spectroscopy, the capacitance being determined according to:

$$C = \frac{\sqrt{(V_g - X)^2 - Y^2}}{2\pi f R\sqrt{X^2 + Y^2}} \sin\left[\arctan\left(\frac{-Y}{V_g - X}\right) - \arctan\left(\frac{Y}{X}\right)\right] \qquad (26)$$

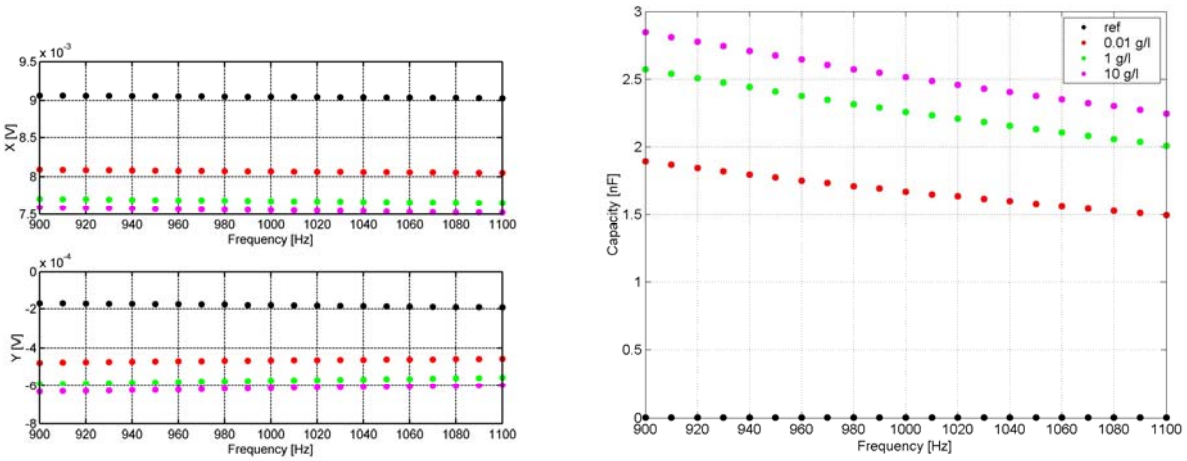

Fig.47 (a) (b)

where *X* and *Y* are the real and imaginary parts of the output signal, measured experimentally, V_g is the input signal, and *f* is the frequency of the input signal. The frequency response of the capacitive detector based on Ni nanowires, for different glucose concentrations of test solutions is presented below as follows:

Fig. 47(a) illustrates the real and imaginary parts of the output signal, and Fig. 47(b) shows the capacitance determined from (26), the concentrations of the test solutions being indicated in the legend.

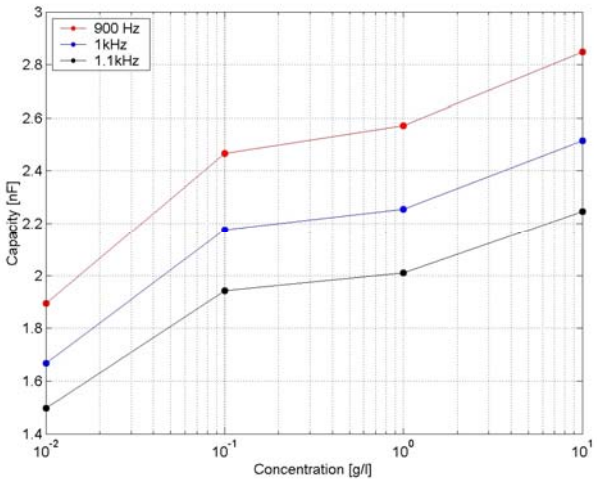

Fig. 48

The calibration curves of the detector in the range of concentrations studied, at different frequencies, are presented in Fig. 48. Due to the large surface/volume ratio and the high catalytic activity of Ni in the glucose oxidation process, the capacitive sensors based on a matrix of Ni nanowires can thus sense glucose successfully.

The application of the Ni nanowire matrix as glucose sensor has been presented at an international conference [C8].

Fabrication of segmented Cu/Ni nanowires

This system is interesting in detecting magnetic fields via the magnetoresistive effect. To fabricate these nanowires we used the technique of sequential deposition from a single electrolytic Watts bath, containing a solution of $NiSO_4 \cdot 6H_2O$ (225 g/l), $NiCl_2 \cdot 6H_2O$ (30 g/l), boric acid (22,5 g/l) and hydrated copper sulphate (4 g/l). The same working configuration as above was used, with three electrodes. Two polarization/voltametric curves recorded successively during the growth of Ni/Cu segmented wires are shown in Fig. 49.

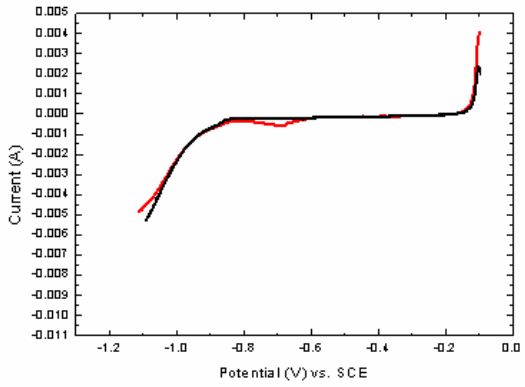

Fig. 49

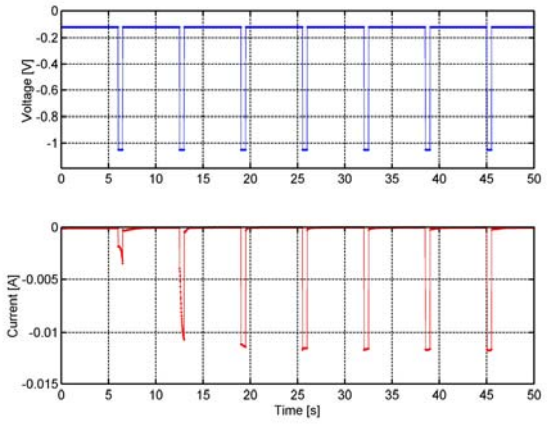

Fig. 50

The relatively flat region in the range (-200 mV, -850 mV) corresponds to the growth of the compound Cu/Ni, while the region (-850 mV, -1200 mV) corresponds to the deposition of a compound significantly richer in Ni (the element with the highest concentration in electrolyte).

The sequential deposition is achieved by controlling the electrode potential in pulses that vary between the values favoring the deposition of one or the other metals (Ni or Cu). Figure 50 presents the programmed sequence of the pulses of the electrode potential (up) and of the deposition current/recorded

chrono-ampermetric curve (bottom). The sequence of pulses is 0.5 s at -1100 mV (potential value that favors the deposition of the metal with the highest concentration in electrolyte, i.e. Ni) and 6.0 s at -120 mV (potential value that favors the deposition of Cu).

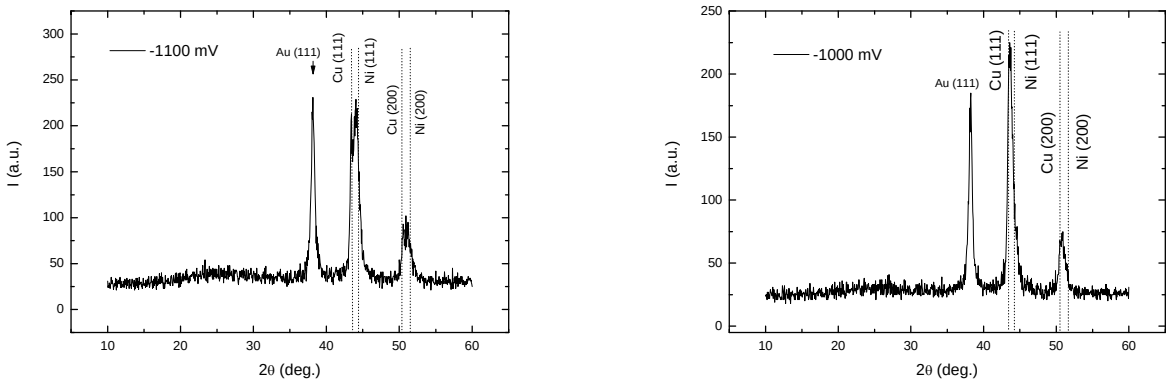

Fig. 51 (a) (b)

The structure of the wires in the obtained matrix was characterized by X-ray diffraction. The diffraction spectra were recorded with a high-resolution diffractometer (Bruker D8 Discover), using the Cu-$K_{\alpha 1}$ radiation (λ= 1.5406 Å) in a grazing incidence configuration, to enhance the optical path of X rays in the sample. The obtained X-ray spectra for two samples with pulse bases at -1100 mV and -1000 mV, respectively, are illustrated in Figs. 51(a) and 51(b). These spectra confirm the increase of Ni content as the potentials have increasingly negative values. The (111) peak of Au is due to the working electrode (substrate).

Results obtained in the 2015 stage of the project

The 2015 stage of the project was focused on the electrical characterization of inhomogeneous and segmented nanowires, similar to those fabricated in 2014 and in which the density of charge carriers/scattering centers vary along the nanowire axis, as well as on the investigation of possible applications of other inhomogeneous distributions of the interaction/scattering potential. The obtained results are detailed in the following.

Electrical characterization of nanowires with an inhomogeneous, segmented distribution of charge carriers/ scattering centers

The numerical simulations obtained in the 2014 stage of the project showed that the segmented nanowires, in which the charge carriers/scattering centers vary stepwise along the nanowire axis, have the greatest potential in electronic and optoelectronic applications. In this respect, in 2014 we have electrochemically grown arrays of Ni/Cu segmented nanowires in the pores of an alumina template. As already mentioned above, these nanowires are able to detect magnetic fields via the magnetoresistive effect.

The template growth method allows the versatile fabrication of nanowires with a controlled diameter [25-28]. We used alumina for growing arrays of segmented Ni/Cu nanowires, the array of pores in alumina being obtained by a controlled anodization process, as described above. Inside the pores in the alumina template, shown in the SEM image in Fig. 1, we have grown segmented nanowires via a relatively low-cost electrochemical procedure, suitable for both metallic and semiconductor nanowires, which does not require sophisticated equipment [29-31]. After the pores are filled, the template can be removed by dissolution in an alkaline solution.

The segmented nanowires were sequentially grown from a single electrolytic Watts-type bath, as detailed above, the growth control being assured by a stepwise variation of the electrode potential between the values that favor the deposition of one or the other metals (Ni or Cu). Figures 52 and 53 represent SEM images of the segmented Ni/Cu nanowires with a diameter of 100 nm, the different segments of the

nanowires being evident in the last image. The X-ray diffraction spectrum in Fig. 54 confirms the presence of both elements, Ni and Cu, in the nanowires. Diffraction peaks attributed to Au and Si are also observable in the X-ray spectrum, the presence of these peaks being justified by the fact that Au is the working electrode and Si is the substrate on which the nanowires are grown.

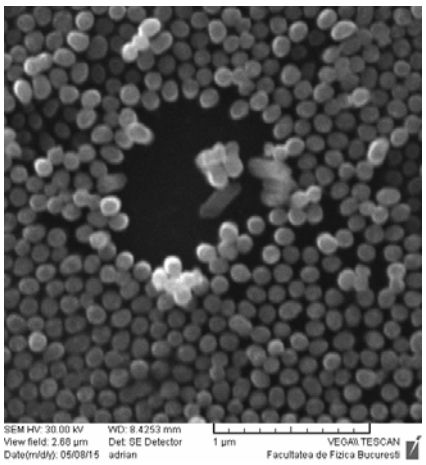

Fig. 52

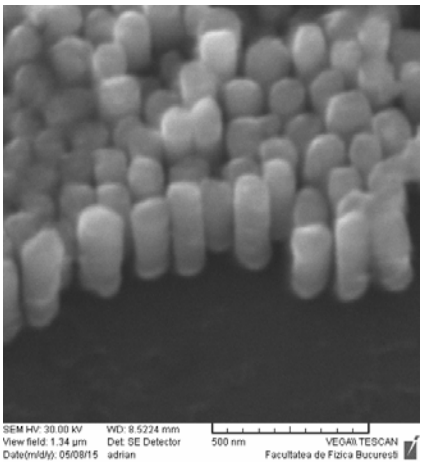

Fig. 53

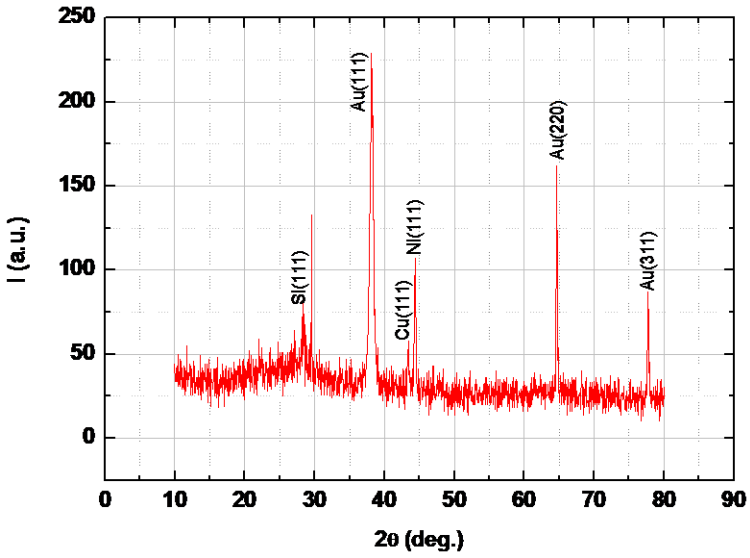

Fig. 54

One of the issues that appeared during electrical measurements was the electric contact with the nanowire arrays. To enhance the quality of the contact, we deposited nanowires higher than the template, in order to form large-area metallic regions above the template. Figures 55 and 56 show the formation of such metallic clusters and, respectively, of a continuous metallic layer above the nanowire array, which can be used as electric contact. The insets in these figures are schematic side representations of the nanowire array grown in the pores of the template, as well as of the clusters/continuous layer above the template. The magenta (brown) segments correspond to Ni (Cu).

As expected, the electrical characterization of the array of segmented nanowires revealed a linear dependence of the current on the applied voltage, the Ni/Cu interface having an ohmic behavior. The electrical resistance, determined from the slope of the current-voltage dependence, has small values, of few ohms, consistent with the conducting behavior of the nanowires. The value of the electrical resistance varies in the presence of an applied magnetic field, as can be seen from Fig. 57, this behavior suggesting the possibility of detecting small magnetic fields, lower than 0.3 T, with the array of Ni/Cu nanowires. These results have been presented at an international conference [C9]. The decrease of the resistance with the magnetic field, of about 1.4%, is caused by the magnetoresistive effect, which was observed also in other segmented nanostructures containing ferromagnetic and diamagnetic materials grown by electrochemnical deposition in the pores of a template [32, 33].

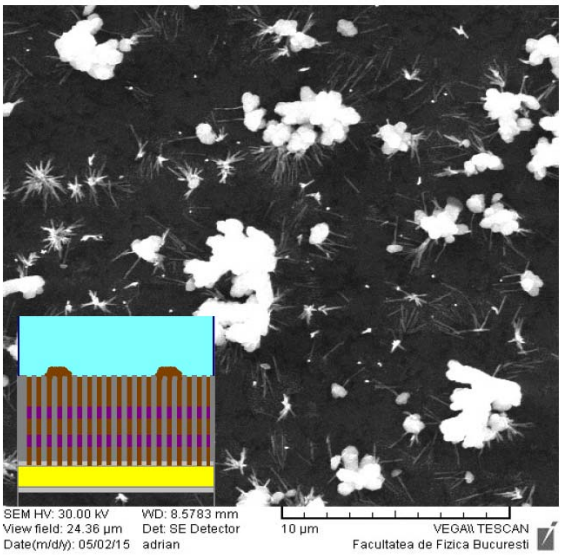

Fig. 55

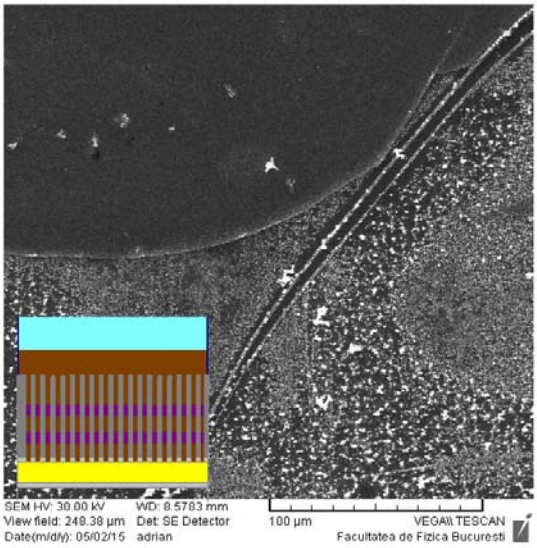

Fig. 56

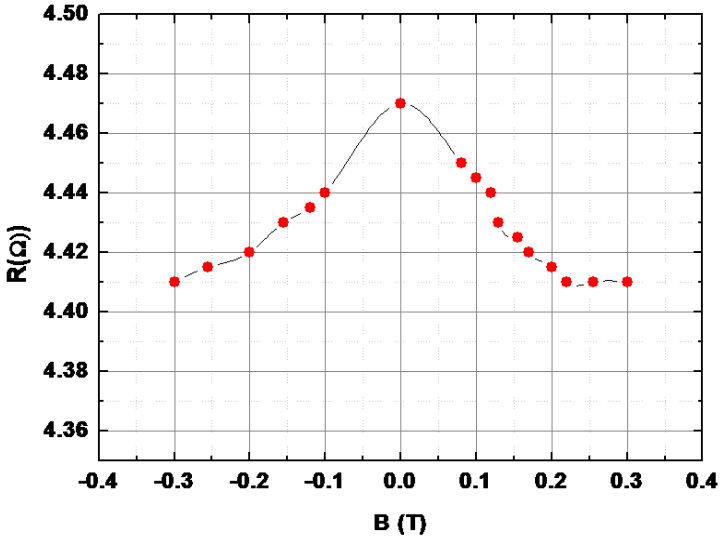

Fig. 57

Ballistic scattering on wrinkled potentials

We considered that it would be beneficial for the project, and, generally, for the advancement of knowledge in the field, to attempt the study of analogies between the propagation of light and ballistic electrons [1, 2] in a wider sense. As such, we investigated ballistic electron propagation through inhomogeneous scattering configurations that attracted less attention recently, in particular through wrinkled potential configurations. We have chosen this configuration based a recent article [34] dedicated to propagation of elastic waves through a region with a wrinkled distribution of refractive indices/elastic coefficients. The aim was to determine the way in which controllable and wrinkled potentials affect the transmission of ballistic electrons in bidimensional semiconductors. In the configuration that we have focused on, illustrated in Fig. 58, the potential energy as well as the number, period and width of the wrinkles in the scattering region can be controlled via a wrinkled gate electrode. Such gate electrodes have been already used in some field-effect transistors [35], or graphene-on-MoS_2 capacitors [36], but no investigation of ballistic propagation (involving phase conservation at reflections/scattering) in such structures exists. Because in the studied configuration a large number of parameters can be varied, we expect an enhanced control on ballistic electron transmission, our study investigating also potential applications of such structures.

The electron transmission coefficient was calculated using the formalism of the R matrix. In our particular case, the scattering region contains a wrinkled scattering potential with a width of 1 nm, which is continued by straight scattering potentials of the same width at the right and left sides of the structure. The variable parameters are: the geometric amplitude of the wrinkle A, its period λ, and the value (positive or negative)

of the scattering potential, denoted by V_0. In all simulations we considered only 5 wrinkles, the length of the wrinkled potential being thus 5λ.

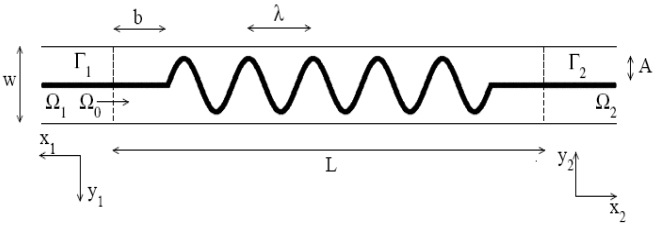

Fig. 58

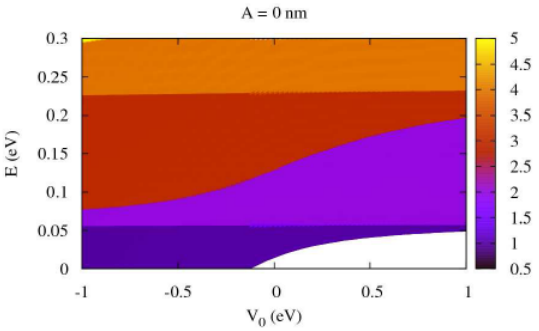

Fig. 59

The propagation of electrons is described by the time-independent Schrödinger equation, in which the uni-particle Hamiltonian in the effective mass approximation is

$$H = -\frac{\hbar^2}{2m}\Delta + W(\boldsymbol{r}), \tag{27}$$

where $\boldsymbol{r} = (x,y)$ is the position vector and the effective mass is $m = 0.0655\ m_0$ (as in GaAs). The studied configuration is that of a bidimensional electron gas (2DEG) with width $W = 20$ nm and length $L = 120$ nm, which includes also straight regions of the scattering potential. The amplitude V_0 of the electrostatic potential can be varied between –1 eV and 1 eV by modifying the gate potential.

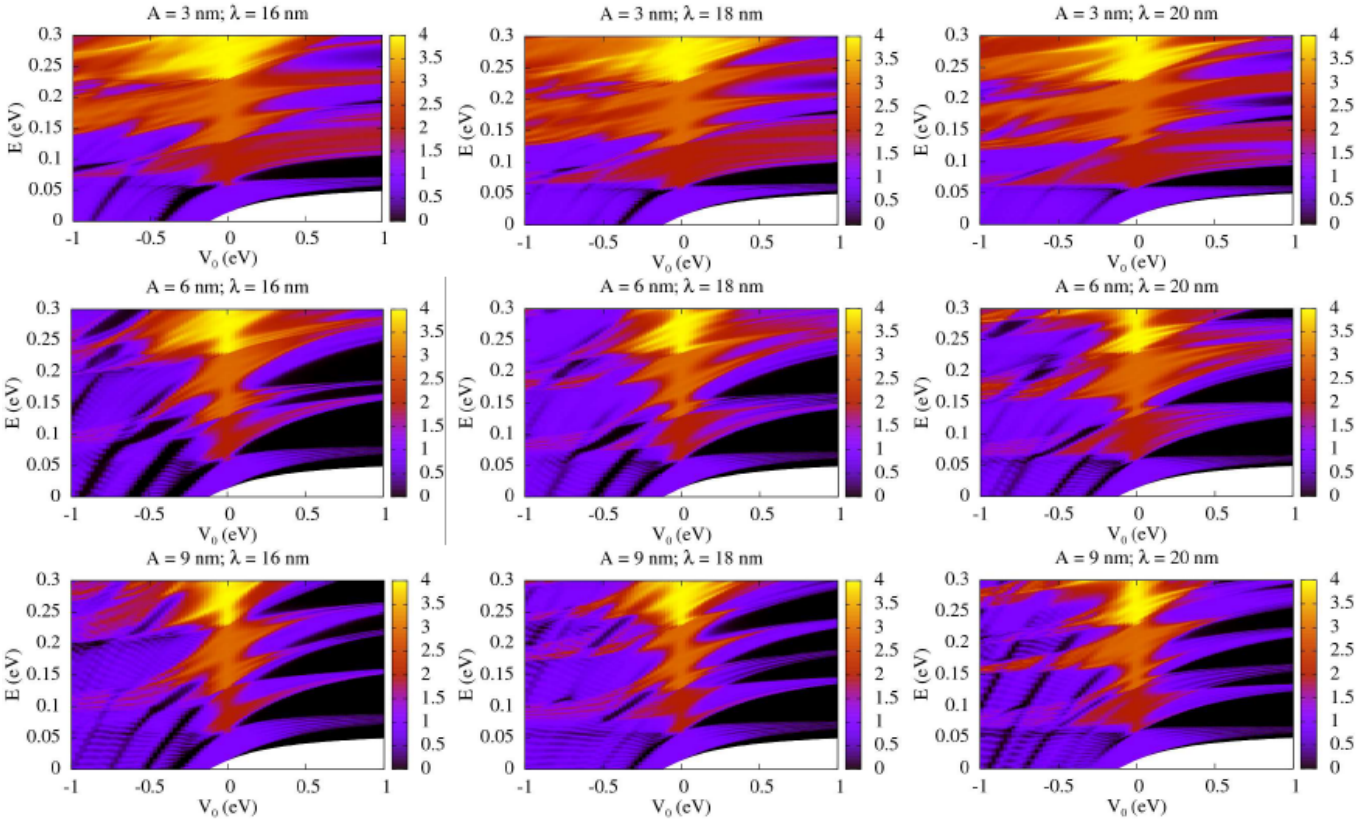

Fig. 60

The dependence of the transmission coefficient, calculated in the R-matrix formalism, on the electron energy E and V_0 is represented in Fig. 59 for $A = 0$ (straight gate) and in Fig. 60 for $A = 3$, 6, and 9 (top, middle and bottom rows, respectively) and $\lambda = 16$ nm, 18 nm and 20 nm (left, middle and right columns, respectively). In all cases, the white region in the lower right corner indicates that electron propagation is forbidden due to the transverse confinement, which imposes a minimum value for the energy of the first

allowed mode in the structure. This minimum energy value depends on V_0 and vanishes for $V_0 < -0.12$ eV, when the spatial confinement effect is absent (a negative potential energy applied by the straight gate electrode, narrower than the 2DEG region, induces an increase of the effective width of the structure, whereas positive V_0 values cause a decrease of the 2DEG effective width).

Figures 59 and 60 indicate different behaviors of the straight and wrinkled scattering potential. In the first case, the transmission increases uniformly with the number of open channels, while in the last case the dependence of the transmission on E and V_0 is more complex, and is also dependent on the sign of V_0.

The shape of the transmission coefficient for positive V_0 values in Fig. 60 can be explained by the formation of minibands in the structure containing periodic potential barriers, the width and location of which shifts towards higher energies as the height of the potential barriers increases [37]. On the other hand, negative V_0 values correspond to a periodic scattering structure with potential wells instead of barriers, structure that favors interferences not only between quantum electron wavefunctions scattered by adjacent wells, but also inside single wells. The superposition of these interferences can generate the complex structure in Fig. 60.

For a better understanding of the difference between the effects of periodic potential barriers and wells on the scattering wavefunction, we have replaced the wrinkled bidimensional scattering potential with a onedimensional potential, consisting of barriers/wells with the same dimensions and heights as those encountered by electrons propagating at different y coordinates in Fig. 58. The equivalent onedimensional configuration is represented in Fig. 61(a), the solid (dotted) thick vertical lines representing the locations of scattering regions for electron trajectories (thin lines of the same type) with $y = 0$ (y different from 0); the solid gray line corresponds to the wrinkled potential. The widths of the onedimensional scattering regions for y different from 0 are larger than for $y = 0$, and their position is no longer equidistant in a period λ, as opposed to the situation when $y = 0$.

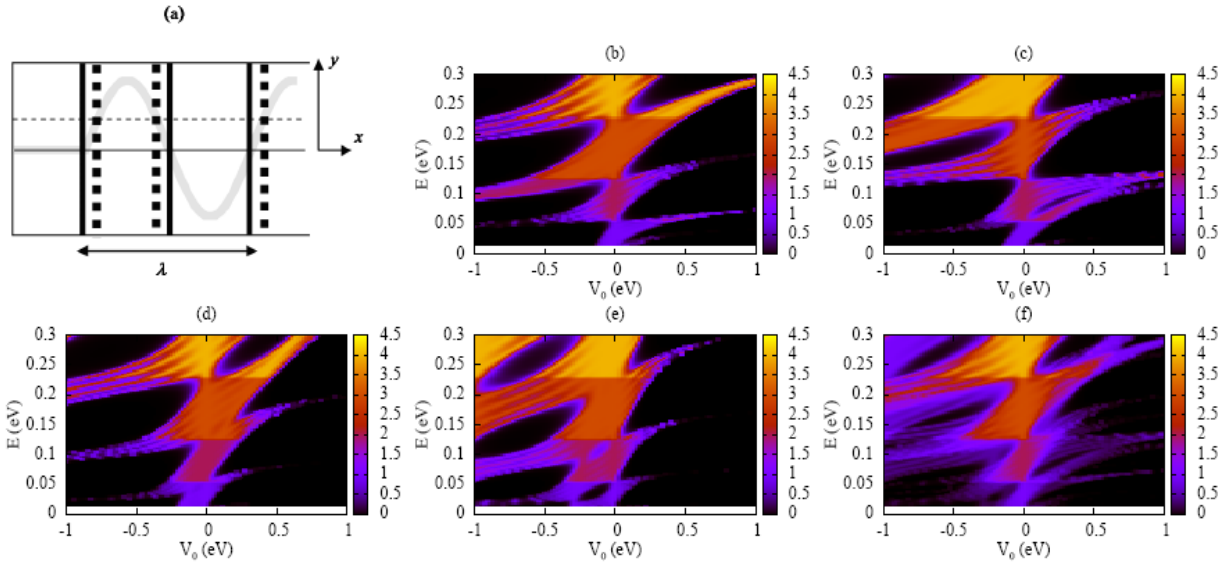

Fig. 61

Figures 61(b)-(e) show the dependence of the transmission coefficient on E and V_0 for trajectories along y = 0, 0.33A, 0.66A and, respectively, 0.85A. Because in the equivalent onedimensional problem the straight continuation to the left and right of the wrinkled scattering potential was not taken into account, the region in which the propagation is forbidden due to the transversal confinement has the same width, independent on V_0. The width of this white region is thus the same as in Fig. 60 for $V_0 = 0$. From figures 61(b)-(e) it can be observed that, although the transmission coefficient shows similar minibands for positive and negative V_0 values, their shape becomes more dissimilar as y (and the width of the scattering regions) increases. Indeed, interferences can form inside sufficiently wide potential wells, as in Fig. 61(e), which then can superimpose the wavefunction interferences between adjacent wells. In this situation, while the transmission is hindered by wide barriers, in regions with positive V_0, for negative values of this parameter

the constructive interferences in wide quantum wells generate significant transmission inside the minibands.

This simple onedimensional model allows an understanding of the transmission coefficient behavior in the bidimensional scattering problem. More precisely, the transmission dependence on E and V_0 in the last case (see Fig. 60) is similar to that in Fig. 61(f), obtained by adding the contributions of trajectories with different y values.

The wrinkled scattering potential affects also the wavefunction in the structure. Propagation examples of the (not normalized) probability distributions in the wrinkled structure for the fundamental mode at two different electron energies are presented in figures 62 and 63 for V_0 = –0.5 eV and, respectively, 0.5 eV. These figures show the effect of the straight left and right continuation of the wrinkled potential on the wavefunction: for the same energy, the wavefunction depends on the attractive (negative V_0) or repulsive (positive V_0) nature of the scattering potential since this is not applied on the entire width of the structure, but only on its central part. In addition, these figures illustrate the effect on the wrinkled scattering potential on the phase of the transmitted wavefunction. For example, in Fig. 62, top, the constructive interferences/wavefunction maxima appear in the center of the structure before the wrinkled region, and are replaced by destructive interferences after scattering. In another example, in Fig. 63, top, the transmitted wavefunction has a similar form as the incident one, but a different oscillation period along x.

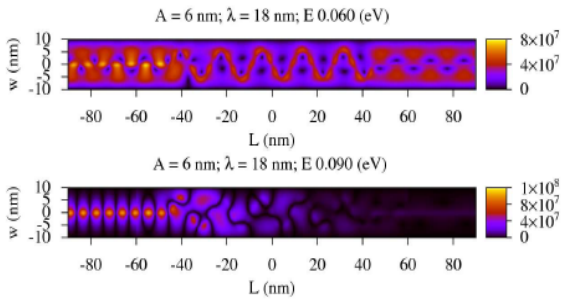

Fig. 62

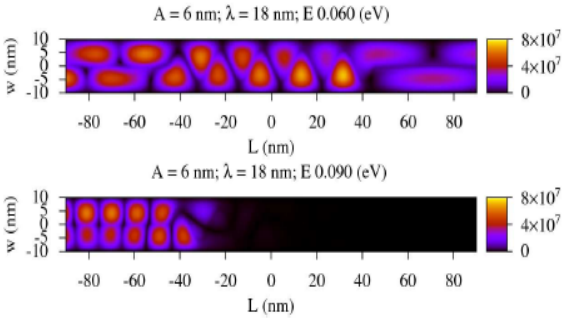

Fig. 63

Numerical simulations show that, for a given form of the scattering potential/gate electrode, the transmission coefficient can be controlled by the applied gate potential. Such a control is not possible/is insignificant in straight scattering potentials with the same widths.

The obtained results emphasize the analogies between the propagation of ballistic electrons and that of electromagnetic waves. If the formation of minibands is well known for light propagation in periodic structures, and is encountered especially in the area of photonic crystal [38], the propagation of electrons through periodic potential wells is analogous to light propagation in anti-resonant reflection optical waveguides (ARROWs) [39]. These structures are less studied, at least from the point of view of ballistic electrons-electromagnetic radiation analogies.

The simulations presented above generalize these analogies and can contribute to the identification of possible applications of wrinkled 2DEG scattering potentials. These results have been published in an ISI journal [P8] and were presented at an international conference [C10].

Results obtained in the 2016 stage of the project

The 2016 stage of the project was dedicated to the comparison between the experimental results obtained in 2014 and 2015, and the numerical simulations (activity 3.4). However, because the segmented nanowire arrays that were electrically characterized in 2015 showed promising results as magnetic field sensors, we have extended their experimental investigation in 2016, in order to study the effect of the nanowire structure on the magnetic response, especially on the magnetoresistance, defined as $\Delta R / R_0$, where $\Delta R = R(B) - R(0)$ and $R_0 = R(0)$, with B the applied magnetic field.

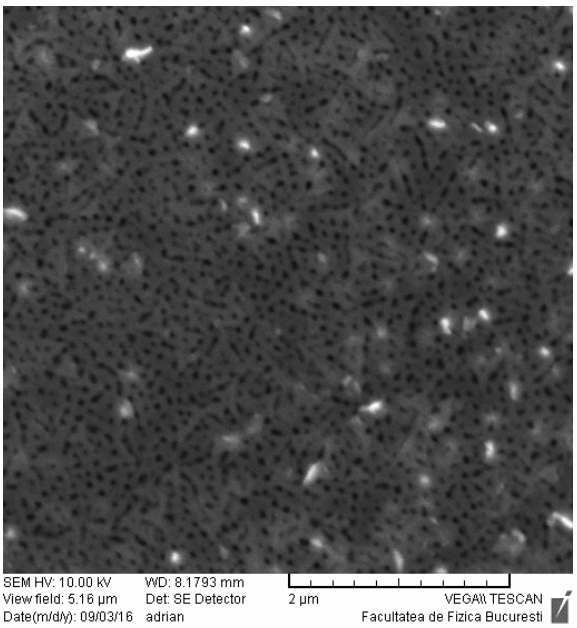

Fig. 64

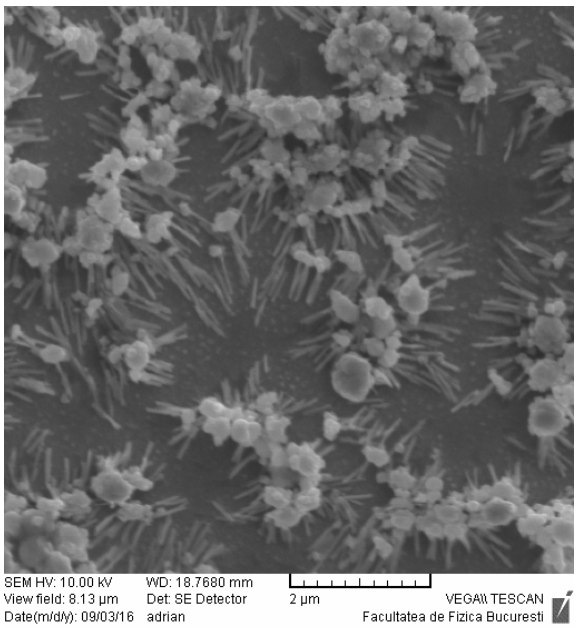

Fig. 65

As a result, we have fabricated new arrays of segmented Ni/Cu nanowires, using the same procedure as described above, with different widths of the Ni+Cu period. More precisely, the fabricated nanowires had an average diameter of 90 nm and a length of 700 nm, which contains either 5 or 10 Ni+Cu periods. SEM images of nanowire arrays grown up to the top of the template and, respectively, forming metallic clusters above the templates are represented in Figs. 64 and 65. These clusters are used for optimum contacting the nanowire arrays.

Typical measurements of the transversal resistance (in a magnetic field normal to the nanowire direction) of the fabricated segmented Ni/Cu nanowire arrays containing 5 and, respectively 10 Ni+Cu periods are shown in Fig. 66(a) and 66(b).

The experimental results confirm the expected increase of magnetoresistance with the magnetic field, as well as the fact that the magnetoresistance is larger for nanowires with a shorter distance between the ferromagnetic Ni segments/shorter periods. The last result, present also in single Ni nanowires or in sparse nanowire arrays, can be explained by a stronger dipolar interaction between closer positioned Ni segments. For Ni segments with small aspect ratio, the coupling between them is dominantly antiferromagnetic, but it changes to mostly ferromagnetic for nanowires with Ni segments with a larger aspect ratio [40]. Regarding the easy magnetization axis, it changes its direction depending on the aspect ratio value, but no agreement on this effect exists yet [40, 41].

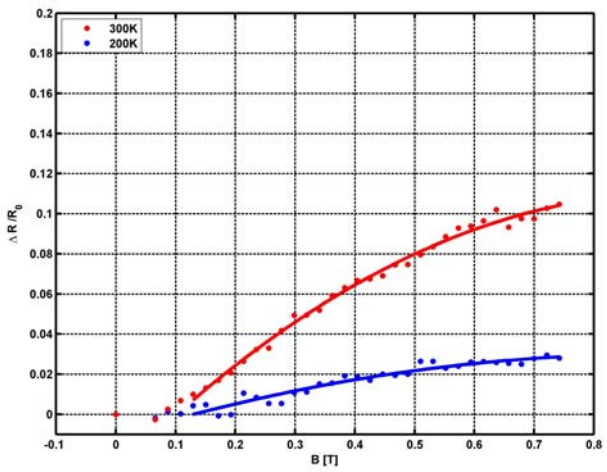

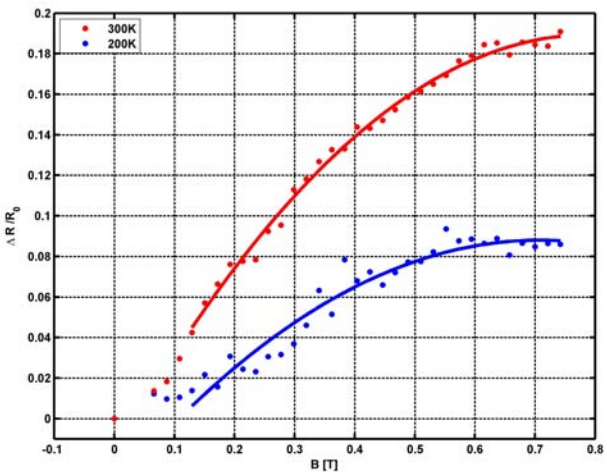

Fig. 66 (a) (b)

On the other hand, in dense arrays of segmented nanowires, as those obtained in this project, significant interactions can develop between Ni segments on adjacent nanowires. Therefore the modeling/prediction of the magnetic response of such a nanowire array is difficult, the experimental results varying from one array to the other, although obtained under similar conditions.

Another controversial effect is the magnetoresistance dependence on temperature. As can be seen from Figs. 66(a)-(b), the room temperature (300 K) magnetoresistance is larger than that measured at lower temperatures, say 200 K. Although such a result is beneficial from the point of view of applications, it does not reflect a usual behavior. Therefore, we have extended the measurements on several nanowire arrays, but the results were not conclusive, the magnetoresistance of some nanowire arrays being positive or negative depending on temperature. An example of such a nanowire array is shown in Fig. 67, the measurement data corresponding to temperatures varying from 100 K and 300 K, with a 50 K step, the lines with lighter colors uniting data obtained at higher temperatures. Because of the dependence of the interaction between Ni segments on the specific configuration of segments in an array, such a result is not surprising.

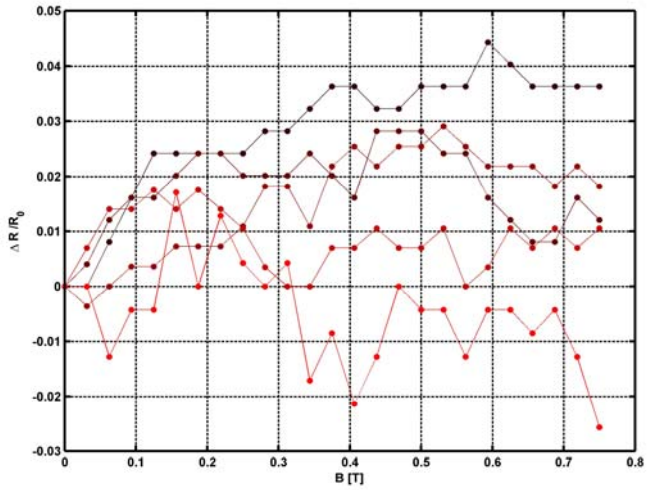

Fig. 67

An extensive bibliographical research identified the cause of magnetoresistance increase in single Ni nanowires and nanowire arrays [42, 43] with a temperature-dependent change of the magnetic anisotropy direction due to the thermal stress originating in different thermal expansion coefficients of Ni nanowires and the surrounding medium. These coefficients generally decrease with the diameter of the nanowires.

Because, as emphasized above, the magnetic response depends on many parameters, additional experimental investigations are required to establish the magnetic response of a certain nanowire array. In addition, the effects of temperature and stress on the contacts must be accounted for, since the nanowires are not contacted individually but via the metallic clusters above the template. Such additional investigations are beyond the scope of the present project.

The results regarding the application of segmented Ni/Cu nanowire arrays as magnetic field detectors were submitted for publication [P9] and were presented at several international conferences [C12, C14-C17].

Regarding the agreement/disagreement between numerical simulations and experimental results, we concluded that:

- the numerical simulations based on the R matrix formalism were applied on semiconducting structures in the ballistic transport regime, in the presence of either attractive or repulsive impurities/scattering centers

- the numerical simulations showed that an inhomogeneous distribution of impurities, even an ordered one, has a similar effect on the charge transport as a random distribution of impurities. The net effect is to attenuate the relative minima and maxima of the transmission coefficient of electrons caused by interferences between wavefunctions reflected by different interfaces, and to favor an almost linear dependence of the current on voltage, typical for a diffusive charge transport

- from an experimental point of view, random and probably inhomogeneous impurity distributions in the nanowires grown in the pores of the alumina template cannot be avoided. As such, it is expected that the charge transport is diffusive, even in semiconducting nanowires. Therefore, the fact that we have investigated metallic nanowires, with a short mean free path, which does not accommodate a ballistic transport regime even at low temperatures, does not affect the comparison with numerical simulations

- thus, theoretical investigations on an inhomogeneous distribution of impurities shows that simulations based the R matrix formalism do not necessarily improve the modeling of the charge transport or magnetic response of segmented Ni/Cu nanowires arrays compared to a (semi)classical/phenomenological treatment

- however, even a phenomenological treatment of the nanowire arrays fabricated during the project cannot provide a satisfactory modeling of the system without additional investigations regarding the relation between the structure/morphology of the nanowire array and its magnetic response. Such investigations are beyond the aim of this project, which focused on analogies between the propagation of light and (quasi)ballistic electrons. In addition, as already mentioned, experimental results on single nanowires or Ni and/or segmented arrays do not agree, an understanding of the magnetic response in such low-dimensional systems depending significantly on the configuration/interaction of Ni segments in the specific sample

- in summary, after investigating the application of Ni/Cu segmented nanowire arrays as magnetic field detectors, we consider that predictive responses can only be obtained in sparse arrays, in which no significant interactions exist between Ni segments on adjacent nanowires. Only in this case we can limit the theoretical study/modeling with some success of the magnetic response of the system to that of an individual nanowire

- on the other hand, it must be emphasized that the R matrix formalism applied to ballistic systems with optical analog lead to interesting theoretical results and practical applications in systems in which the distribution of scattering centers is periodic. For instance, a novel method was suggested for modulating the electron transmission via positive or negative voltages applied on a wrinkled gate, narrower than the two-dimensional electron gas

- even for interfaces between homogeneous media, the light-ballistic electrons analogy lead to unexpected applications. For example, we have shown during this project that ballistic electrons can be steered by a simple interface between a material with an isotropic effective mass tensor and another one with a tilted non-isotropic effective mass tensor

- the last two theoretical predictions could not be demonstrated experimentally during the project, the technology necessary for fabricating the devices suggested by numerical simulations being not available in the research center in which the project was implemented

- in conclusion, we consider that the experimental results obtained during the project can be described by theoretical models (even phenomenological in some cases) and can be simulated with the developed algorithms if the magnetic interactions between the ferromagnetic Ni segments in the pores of the template are known. This knowledge requires, however, additional investigations, far beyond the aim of the present project. On the other hand, based also on bibliographical references, we consider that the computing algorithms developed during this project can simulate the charge transport in systems with arbitrary, including inhomogeneous, distributions of scattering centers, and that the results predicted by the theoretical simulations performed during this project can and will be demonstrated experimentally using advanced technologies

References

[1] G.N. Henderson, T.K. Gaylord, E.N. Glytsis, Proc. IEEE 79, 1643 (1991).
[2] D. Dragoman, M. Dragoman, Progress in Quantum Electronics 23, 131 (1999).
[3] B.E.A. Saleh, M.C. Teich, *Fundamentals of Photonics*, 2nd edition, Wiley-Interscience (2007).
[4] A.H. Castro Neto, F. Guinea, N.M.R. Peres, K.S. Novoselov, A.K. Geim, Rev. Mod. Phys. 81, 109 (2009).
[5] D. Dragoman, J. Opt. Soc. Am. B 27, 1325 (2010).
[6] I. Mihalache, D. Dragoman, J. Opt. Soc. Am. B 28, 1746 (2011).
[7] H. Luo, W. Hu, X. Yi, H. Liu, J. Zhu, Opt. Commun. 254, 353 (2005).

[8] D. Dragoman, M. Dragoman, Phys. Lett. A 210, 121 (1996).
[9] D. Dragoman, M. Dragoman, J. Appl. Phys. 101, 104316 (2007).
[10] Yu.A. Bychkov, E.I. Rashba, J. Phys. C 17, 6039 (1984).
[11] S.D. Ganichev, et al., Phys. Rev. Lett. 92, 256601 (2004).
[12] A. Erdoglu, *Wave Propagation and Radiation in Gyrotropic and Anisotropic Media*, Springer, New York (2010).
[13] D. Dragoman, Opt. Commun. 284, 2095 (2011).
[14] R.A. Sepkhanov, Ya.B. Bazaliy, C.W.J. Beenakker, Phys. Rev. A 75, 063813 (2007).
[15] D. Dragoman, M. Dragoman, J. Appl. Phys. 110, 014302 (2011).
[16] C.W.J. Beenakker, in *Oxford Handbook of Random Matrix Theory*, G. Akemann, J. Baik, P. Di Francesco, Eds., Oxford Univ. Press (2011).
[17] A. Yamilov, B. Payne, J. Mod. Opt. 57, 1916 (2010).
[18] H. Cao, J.Y. Xu, D.Z. Zhang, S.-H. Chang, S.T. Ho, E.W. Seelig, X. Liu, R.P.H. Cheng, Phys. Rev. Lett. 84, 5584 (2000).
[19] N. Neophytou, X. Zianni, H. Kosina, S. Frabboni, B. Lorenzi, D. Narducci, J. Electron. Mater., doi: 10.1007/s11664-013-2898-z
[20] X. Mo, T. Mizokuro, C. Heck, N. Tanigaki, T. Hiraga, Nano-Micro Lett. 1, 19 (2009).
[21] P. Saha, S. Basu, J. Electron Dev. 15, 1254 (2012).
[22] J. He, X. Xi, M. Chan, C. Hu, Y. Li, Z. Xing, R. Huang, Semicond. Sci. Technol. 17, 721 (2002).
[23] N. Debbar, H. Al-Hokail, Int. J. Electronics 87, 1153 (2000).
[24] M.G.A. Crawford, P.W. Brouwer, C.W.J. Beenakker, Phys. Rev. B 67, 115313 (2003).
[25] D.D. Li, R.S. Thomson, G. Bergmann, J.G. Lu, Adv. Mater. 20, 4575 (2008).
[26] H. Masuda, K. Fukuda, Science 268, 1466 (1995).
[27] C. Tazlaoanu, L. Ion, I. Enculescu, M. Sima, M. Enculescu, E. Matei, R. Neumann, R. Bazavan, D. Bazavan, S. Antohe, Physica E 40, 2504 (2008).
[28] M. Ghenescu, L. Ion, L. Enculescu, C. Tazlaoanu, V.A. Antohe, M. Sima, M. Enculescu, E. Matei, R. Neumann, O. Ghenescu, V. Covlea, S. Antohe, Physica E 40, 2485 (2008).
[29] E. Matei, L. Ion, S. Antohe, R. Neumann, I. Enculescu, Nanotechnology 21, 105202 (2010).
[30] V.A. Antohe, A. Radu, M. Matefi-Tempfli, A. Attout, S. Yunus, P. Bertrard, A. Dutu, A. Vlad, S. Melinte, S. Matefi-Tempfli, L. Piraux, Appl. Phys. Lett. 94, 073118 (2009).
[31] E. Matei, I. Enculescu, M.E. Toimil-Molares, A. Leca, C. Ghica, V. Kuncser, J. Nanopart. Res. 15, 1863 (2014).
[32] X.-T. Tang, G.-C. Wang, M. Shima, J. Appl. Phys. 99, 033906 (2006)
[33] K.Y. Kok, C.M. Hangarter, B. Goldsmith, I.K. Ng, N.B. Saidin, N.V. Myung, J. Magnetism and Magnetic Materials 322, 3876 (2010).
[34] S. Rudykh, M.C. Boyce, Phys. Rev. Lett. 112, 034301 (2014).
[35] A. Poghossian, K. Schumacher, J.P. Kloock, C. Rosenkranz, J.W. Schultze, M. Müller-Veggian, M.J. Schöning, Sensors 6, 397 (2006).
[36] A.V. Kretinin, Y. Cao, J.S. Tu, G.L. Yu, R. Jalil, K.S. Novoselov, S.J. Haigh, A. Gholinia, A. Mishchenko, M. Lozada, T. Georgiou, C. Woods, F. Withers, P. Blake, G. Eda, A. Wirsig, C. Hucho, K. Watanabe, T. Taniguchi, A.K. Geim, R.V. Gorbachev, Nano Lett. 14, 3270 (2014).
[37] P. Vasilopoulos, F.M. Peeters, D. Aitelhabti, Phys. Rev. B 41, 10021 (1990).
[38] K. Sakoda, *Optical Properties of Photonic Crystals*, Springer (2005).
[39] N.M. Litchinitser, A.K. Abeeluck, C. Headley, B.J. Eggleton, Opt. Lett. 27, 1592 (2002).
[40] M. Susano, M.P. Proenca, S. Moraes, C.T. Sousa, J.P. Araújo, Nanotechnology 27, 335301 (2016).
[41] M. Chen, C.-L. Chien, P.C. Searson, Chem. Mater. 18, 1595-1601 (2006).
[42] Y. Rheem, B.-Y. Yoo, W.P. Beyermann, N.V. Myung, Nanotechnology 18, 015202 (2007).
[43] D. Navas, K.R. Pirota, P. Mendoza Zelis, D. Velazquez, C.A. Ross, M. Vazquez, J. Appl. Phys. 103, 07D523 (2008).

Scientific publications related to the project:

a) papers in ISI journals:

[P1] D. Dragoman – Influence of light polarization on the analogy between ballistic nanostructures and the electromagnetic field, J. Opt. Soc. Am. B 29, 1528-1534 (2012).

[P2] A. Radu, D. Dragoman, S. Iftimie – Steering and collimating ballistic electrons with amphoteric refraction, J. Appl. Phys. 112, 024318 (2012).

[P3] A. Dumitriu, D. Dragoman – Composite metamaterial for ballistic electrons, J. Phys. D 45, 485104 (2012).

[P4] D. Dragoman, A. Radu, S. Iftimie – Optical analogues of chiral fermions in graphene, J. Opt. 15, 035710 (2013).

[P5] D. Dragoman – Dirac-Schrödinger transformations in contacted graphene structures, J. Appl. Phys. 113, 214312 (2013).

[P6] D. Dragoman – Optical analogues of nanostructures with Rashba-Dresselhaus interactions, J. Opt. 16, 015710, 2014

[P7] T.L. Mitran, G.A. Nemnes, L. Ion, D. Dragoman – Effects of graded distribution of scattering centers on ballistic transport, J. Appl. Phys. 116, 124316, 2014

[P8] T.L. Mitran, G.A. Nemnes, L. Ion, D. Dragoman – Ballistic electron transport in wrinkled superlattices, Physica E 81, 131-135, 2016

[P9] A. Radu, S. Iftimie, L. Ion, S. Antohe, D. Dragoman – Ni-based nanowire arrays as chemical and magnetic field sensors, trimisă spre publicare

b) contributions at international conferences/workshops:

[C1] A. Radu, S. Iftimie, D. Dragoman – Manipulating ballistic electrons by refraction at an interface between isotropic and anisotropic media, Proc. of 35th International Semiconductor Conf., Sinaia, Romania, 2012, pp. 113-116

[C2] A. Dumitriu, D. Dragoman – Ballistic electron propagation in a composite metamaterial, Proc. of 35th International Semiconductor Conf., Sinaia, Romania, 2012, pp. 487-490

[C3] S. Iftimie, A. Radu, D. Dragoman – Optical testing of ballistic transport in graphene devices, EMRS 2012 fall meeting, Poster: http://www.emrs-strasbourg.com/files/FALL%2012/symposium_g.pdf

[C4] D. Dragoman – Classical optical analogies of ballistic charge carriers in graphene, 518. WE Heraeus Seminar on Quantum-Optical Analogies: a Bridge Between Classical and Quantum Physics, lucrare invitata http://www.mpl.mpg.de/en/leuchs/conferences/we-heraeus-seminar-2012.html

[C5] S. Iftimie, A. Radu, D. Dragoman – Optical analogies of quantum chirality, 518. WE Heraeus Seminar on Quantum-Optical Analogies: a Bridge Between Classical and Quantum Physics, Poster http://www.mpl.mpg.de/en/leuchs/conferences/we-heraeus-seminar-2012.html

[C6] T.L. Mitran, L. Ion, D. Dragoman – Ballistic transport in disordered nano-ribbons, Proc. of 36th International Semiconductor Conf., Sinaia, Romania, 2013, pp. 251-254

[C7] T.L. Mitran, G.A. Nemnes, L. Ion, S. Iftimie, A. Radu, D. Dragoman – Ballistic scattering on nanoribbons with controlled disorder, EMRS 2014 Fall Meeting, 15-19 Sept., Warsaw, Poland

[C8] A. Radu, S. Iftimie, T.L. Mitran, L. Ion, D. Dragoman – Ni nanowire arrays as glucose sensor, EMRS 2014 Fall Meeting, 15-19 Sept., Warsaw, Poland

[C9] A. Radu, S. Iftimie, T.L. Mitran, L. Ion, S. Dulcea, M. Mitrea, S. Antohe, D. Dragoman – Tunable magnetic response of segmented Cu/Ni nanowires, E-MRS (European Materials Research Society) Spring Meeting, 11-15 May 2015, Lille, France

[C10] T.L. Mitran, G.A. Nemnes, L. Ion, D. Dragoman – Ballistic electron transport in wrinkled metamaterials, 8th International Conference on Advanced Materials (ROCAM 2015), 7-10 July 2015, Bucharest, Romania

[C11] D. Dragoman – Analogies between light and electrons in nanostructures. Applications, TIM 15-16 Physics Conference, 26-28 May 2016, Timisoara, Romania (invited contribution)

[C12] A. Radu, S. Iftimie, L. Ion, S. Antohe, D. Dragoman – Study of magnetic response of segmented Cu/Ni nanowires, TIM 15-16 Physics Conference, 26-28 May 2016, Timisoara, Romania

[C13] D. Dragoman – Light-inspired ballistic nanostructure configurations, 16th International Balkan Workshop on Applied Physics and Materials Science, 7-9 July 2016, Constanta, Romania (plenary)

[C14] S. Iftimie, A. Radu, A.I. Calugar, B. Bita, L. Ion, S. Antohe, D. Dragoman – Study of physical properties of Ni:Cu segmented nanowires for sensing devices, 16th International Balkan Workshop on Applied Physics and Materials Science, 7-9 July 2016, Constanta, Romania

[C15] A. Radu, S. Iftimie, A.I. Calugar, L. Ion, S. Antohe, D. Dragoman – Optimization of metallic segmented nanowires fabrication process using Al_2O_3 template, 16th International Balkan Workshop on Applied Physics and Materials Science, 7-9 July 2016, Constanta, Romania

[C16] S. Iftimie, A. Radu, A.I. Calugar, B. Bita, L. Ion, S. Antohe, D. Dragoman – Study of morphological, structural and electrical properties of Ni:Cu segmented nanowires, 11th International Conf. on Physics of Advanced Materials, 8-14 Sept. 2016, Cluj-Napoca, Romania

[C17] A. Radu, S. Iftimie, A.I. Calugar, A.-M. Raduta, L. Ion, S. Antohe, D. Dragoman – Optimization growth procedure of metallic segmented Ni nanowires for sensing devices, 11th International Conf. on Physics of Advanced Materials, 8-14 Sept. 2016, Cluj-Napoca, Romania

Project Director,
Prof.dr. Daniela Dragoman